ARL-TR-9125 ● Dec 2020

Hybrid Experimental-Modeling-Computational (HEMC) Concept: Determine Skull Fracture

by Tusit Weerasooriya and Stephen L Alexander

Approved for public release; distribution is unlimited.

NOTICES

Disclaimers

The research reported in this document was performed in connection with contract/instrument W911QX-16-D-0014 with the DEVCOM Army Research Laboratory.

The findings in this report are not to be construed as an official Department of the Army position unless so designated by other authorized documents. The views and conclusions contained in this document are those of SURVICE Engineering Company and the DEVCOM Army Research Laboratory.

Citation of manufacturer's or trade names does not constitute an official endorsement or approval of the use thereof.

Destroy this report when it is no longer needed. Do not return it to the originator.

ARL-TR-9125 ● DEC 2020



Hybrid Experimental-Modeling-Computational Concept: Determine Skull Fracture

Tusit Weerasooriya
Weapons and Materials Research Directorate, DEVCOM Army Research Laboratory

Stephen L Alexander
SURVICE Engineering Company

Approved for public release; distribution is unlimited.

REPORT DOCUMENTATION PAGE

Form Approved
OMB No. 0704-0188

Public reporting burden for this collection of information is estimated to average 1 hour per response, including the time for reviewing instructions, searching existing data sources, gathering and maintaining the data needed, and completing and reviewing the collection information. Send comments regarding this burden estimate or any other aspect of this collection of information, including suggestions for reducing the burden, to Department of Defense, Washington Headquarters Services, Directorate for Information Operations and Reports (0704-0188), 1215 Jefferson Davis Highway, Suite 1204, Arlington, VA 22202-4302. Respondents should be aware that notwithstanding any other provision of law, no person shall be subject to any penalty for failing to comply with a collection of information if it does not display a currently valid OMB control number.
PLEASE DO NOT RETURN YOUR FORM TO THE ABOVE ADDRESS.

1. REPORT DATE *(DD-MM-YYYY)*	2. REPORT TYPE	3. DATES COVERED (From - To)
December 2020	Technical Report	1 October 2018–30 September 2019

4. TITLE AND SUBTITLE
Hybrid Experimental-Modeling-Computational (HEMC) Concept: Determine Skull Fracture

5a. CONTRACT NUMBER

5b. GRANT NUMBER

5c. PROGRAM ELEMENT NUMBER

6. AUTHOR(S)
Tusit Weerasooriya and Stephen L Alexander

5d. PROJECT NUMBER

5e. TASK NUMBER

5f. WORK UNIT NUMBER

7. PERFORMING ORGANIZATION NAME(S) AND ADDRESS(ES)
DEVCOM Army Research Laboratory
ATTN: FCDD-RLW-PB
Aberdeen Proving Ground, MD 21005-5066

8. PERFORMING ORGANIZATION REPORT NUMBER
ARL-TR-9125

9. SPONSORING/MONITORING AGENCY NAME(S) AND ADDRESS(ES)

10. SPONSOR/MONITOR'S ACRONYM(S)

11. SPONSOR/MONITOR'S REPORT NUMBER(S)

12. DISTRIBUTION/AVAILABILITY STATEMENT
Approved for public release; distribution is unlimited.

13. SUPPLEMENTARY NOTES
ORCID ID: Tusit Weerasooriya, 0000-0003-3299-2166

14. ABSTRACT

Impact thresholds for different mechanisms of functional impairments to the brain at cellular or tissue scale would be the preferred method to predict head injuries, but establishing such a comprehensive capability to understand dominant possible injury mechanisms under multi-axial stress-states and rates is currently not available. Until then, skull fracture could serve as an indication of head injury; thus, the ability to predict the initiation of skull fracture through finite element simulation can serve as an in silico tool for assessing various head-protection scenarios. Here, a concept previously developed for uniaxial compression was extended to represent the multi-axial loading condition of the in vivo skull by considering possible different dominant failure mechanisms of fracture during any low-rate impact event to the head, while also incorporating the influence of the heterogeneous microstructural details. A microstructurally inspired mechanism-based failure surface was used for failure thresholds, representing fracture initiation from different dominant mechanisms of skull failure. The failed cracked structure predicted by the simulation represented remarkably well the crack pattern from the corresponding experiment, when visualized through 3-D tomography, thus validating the implemented hybrid experimental-modeling-computational concept.

15. SUBJECT TERMS
skull fracture, skull mechanics, skull modulus, skull failure, skull fracture mechanisms, skull microstructure-property relationship, head injury criteria, hybrid experimental-modeling-computational, HEMC, backface deformation

16. SECURITY CLASSIFICATION OF:			17. LIMITATION OF ABSTRACT	18. NUMBER OF PAGES	19a. NAME OF RESPONSIBLE PERSON
a. REPORT	b. ABSTRACT	c. THIS PAGE			Tusit Weerasooriya
Unclassified	Unclassified	Unclassified	UU	72	19b. TELEPHONE NUMBER (Include area code) 410-652-9450

Standard Form 298 (Rev. 8/98
Prescribed by ANSI Std. Z39.18

Contents

List of Figures v

List of Tables ix

Preface x

Acknowledgments xi

Executive Summary xii

1. Introduction 1

2. Methods 6

2.1 Specimen Extraction and Quasi-Static Indentation Experiment 6

2.2 Microstructurally Inspired and Mechanism-Based (MIMB) Model of Failure in the Human Skull 8

2.2.1 Dominant Mechanisms of Initiation of Skull Failure during Indent Loading 8

2.2.2 Microstructurally Inspired 12

2.3 Finite-Element Simulation 12

3. Results 19

4. Discussion 24

4.1 Comparing Values for the Young's Modulus and Strength of the Human Skull 25

4.2 Inter-Study Comparisons Hindered by Different Experimental Techniques and the Inapplicability of Coupon-Derived Values to Describe Multi-Axial Loading Scenarios 30

4.3 Limitations and Assumptions 31

5. Conclusion and Future Work 33

6. References 35

Appendix A. Parametric Study of the Modulus and Failure Strength Power Relationships **40**

Appendix B. Effect of the Finite (Non-Quasi-Static) Velocity of Indenter/Impactor **47**

Appendix C. Effect of Changing the Indenter/Impactor Point of Contact with the Skullcap (POI) **50**

List of Symbols, Abbreviations, and Acronyms **54**

Distribution List **55**

List of Figures

Fig. 1 Overview of previous experimental mechanical characterization of the human skull. Authors include Alexander et al. (2019, 2020a), Brown et al.* (2020), McElhaney et al. (1970), Motherway et al.** (2009), and Robbins and Wood (1969). Asterisk (*) indicates the reported strain rates were obtained from displacement rate of the shearing punch divided by the gage length of the total specimen in the loading direction. Double asterisk (**) indicates that the method of obtaining these reported constant strain rates was not defined. 2

Fig. 2 Skullcap specimen: A) example of a typical skullcap specimen after extraction from the top part of the skull, B) top-down view of the skullcap specimen used in the current study, showing the outer surface (nearest to the skin), and C) cross-sectional micro-CT image of the skullcap specimen, with gray representing bone and black representing pores or the surrounding medium 7

Fig. 3 The three dominant initiation mechanisms of skull failure—linear fracture, depressed fracture, and shear plug fracture—are represented together with their correlated stress thresholds: tensile, compressive, and shear, respectively. Subsequent failure after initiation could be mixed-fracture of these dominant mechanisms. The specific mechanism (M) by which the skull fails in a given loading condition is assumed to be a function of the velocity (V_{proj}) and geometry of the projectile, specifically its radius of curvature (R_{curv}) and effective diameter (D_{eff}). (Unpublished skull and helmet pictures courtesy of Karin Rafaels, ARL; depressed and mixed fracture pictures are public domain from the National Institutes of Health [NIH]) 9

Fig. 4 Proposed failure mechanism map for human skull shown in the plane of principal stress and max shear-stress (unpublished pictures of fractured skulls courtesy of Karin Rafaels, ARL; depressed and mixed fracture pictures are public domain from the NIH). A rectangle failure surface is purposed: the skull is predicted to fail if the stress-state falls outside the rectangle, but does not fail if it remains within the rectangle. Failure by linear fracture is assumed when the maximum principal stress exceeds its threshold (right-hand bounds of the rectangle), in depressed fracture when the magnitude of the minimum principal stress exceeds its threshold (left-hand bounds of the rectangle), and by shear plug penetration when the magnitude of the maximum shear stress exceeds its threshold (top and bottom bounds of the rectangle). The thresholds are microstructure-dependent, calculated from the BVF by power-laws. Three examples are shown for BVF values of BVF = 0.50 (inner purple rectangle), BVF = 0.75 (dark blue), and BVF = 1.0 solid bone (light blue). The thresholds for these BVF examples were calculated using relationships previously published from experiments on human skull coupons (Boruah et al. 2017, Alexander et al. 2020a, Brown et al. 2020). 11

Fig. 5 Skullcap simulation geometry. A) skullcap resting on the backing plate, together with the indenter/impactor at the POI. B) Top-down view of the specimen, where the gradient in element sizes is clearly visible from largest at the perimeter to smallest under the POI. (C) Anterior–posterior cross section of the specimen under the POI. In all subfigures, the elements of the specimen are color-coded by BVF, as indicated in the color bar in (C). Indenter/impactor diameter was 31.75 mm. Maximum transverse dimensions of skullcap: y = 88.86 mm and x = 71.97 mm. 14

Fig. 6 VUMAT flowchart showing process for calculating the stress for a given element at the timepoint t = i. Element status is tracked via a state-dependent variable, abbreviated here as SDV1..... 16

Fig. 7 Effect of power-law coefficients on the load-displacement response of the skullcap simulation as compared with the experiment. Displacement is measured as the amount of indentation ("applied indentation") of the indenter into the specimen. The crosshead load is measured directly from the test machine in the experiments. The load in the simulations is measured as the reaction force of the indenter in the indentation direction. The final optimized parameter values were used in Simulation 4..... 20

Fig. 8 Failure mechanism map, comparing the failure locus from initial values for the thresholds (light green rectangle, as in Fig. 4) with the final values used in Simulation 4 (dark green rectangle)..... 21

Fig. 9 Load-displacement of Simulation 4 (as in Fig. 7) plotted with the number of elements that failed by compression, tension, or shear 22

Fig. 10 Comparison of cracking pattern on the specimen backface between experiment and Simulation 4. The experimental cracking pattern is visible in comparing the pre-experiment and post-experiment micro-tomographs (left and right). Dotted line indicates location of cross-sectional images in Fig. 11. Cracking pattern from simulation is visualized by color-coding the elements in the undeformed mesh by their active/failed status at the end of Simulation 4. Element color code matches the colors used in the VUMAT flowchart in Fig. 6 (red = failed in tension, gold = failed in compression, and green = failed in shear). Inset shows overlapping predicted and post-crack patterns, which are remarkably similar on the backface. 23

Fig. 11 Comparison of cracking pattern on a cross section (x-z) of the specimen. Location of cross-sectional cut was shown as red dashed line in Fig. 10. Elements in the simulation are color-coded to show active/failed status as in Fig. 10. 24

Fig. 12 Modulus power relationships for the human skull, comparing the relationship optimized from the human skullcap simulation (dashed line) with previous relationships (solid lines). Two of the previous relationships were derived from experiments on other bones apart from the skull (Carter and Hays 1977; Zannoni 1999). These are included since they were subsequently used in FE simulations of the skull (Motherway 2012; Chamrad et al. 2018; Haen et al. 2018)..... 26

Fig. 13 Power relationships for failure strength of human skull bone. The parameters inversely derived in the present study (solid lines without markers) are compared with previously published experimental relationships on human skull bone (triangular markers). Note the relationship from Brown et al. (2020) shown here was for the shear ultimate stress..... 27

Fig. A-1 Summary of load-displacement effect of changing the power-law relationship parameters (Table A-1). 42

Fig. A-2 Effect of changing the leading coefficient ($\mathbf{E_0}$) of the power law for the modulus. For these three simulations, the compressive and tensile failure power relationships were given by $\boldsymbol{\sigma_f^c} = \boldsymbol{\sigma_f^t}$ =175*BVF$^{2.0}$, and there was no shear failure considered. 43

Fig. A-3 Number of elements failed in compression and tension as a function of applied indentation for Simulation 2. Skullcap rupture at an applied indentation of 1.71 mm corresponded with a sharp increase in the number of elements that failed in tension. Therefore, Simulation 3 used a higher value for leading coefficient of the tensile-failure power relationship..... 44

Fig. A-4 Effect of changing the leading coefficient of the power law for tensile failure. For both of these simulations, the modulus power relationship was E = 3.0*BVF$^{2.0}$ GPa; the compressive power relationship was $\boldsymbol{\sigma_f^c}$ = 175*BVF$^{2.0}$ MPa, and no shear failure was considered..... 45

Fig. A-5 Effect of changing the leading coefficient of the power law for shear failure. For all of these simulations, the modulus power relationship was E = 3.0*BVF$^{2.0}$ GPa, the compressive failure power relationship was $\boldsymbol{\sigma_f^c}$ = 175*BVF$^{2.0}$ MPa, and the tensile failure power relationship was $\boldsymbol{\sigma_f^t}$ = 269.4*BVF$^{2.0}$ MPa..... 46

Fig. B-1 Ratio of KE to total energy during the simulation of skullcap indentation, together with the simulation load displacement..... 49

Fig. C-1 Top-down view of the skullcap mesh with the original and changed POI locations marked. Distance in the x-y plane between the two POI locations was 7.63 mm..... 51

Fig. C-2 Effect on the load-displacement response of Simulation 4 by changing the POI. Simulation with the changed POI (orange curve) aborted early at u_y = 2.23 mm due to element distortion. 52

Fig. C-3 Effect on the backface cracking pattern of changing the POI. The meshes are in the undeformed configuration prior to the start of the simulation. Elements are color-coded by active/failed status for the time point corresponding to an applied displacement of u_y = 2.23 mm. 53

List of Tables

Table 1 BVF-property relationship values for human skull 24

Table 2 Failure strengths (megapascals) for the cortical bone of the human skull (outer and inner tables)..... 29

Table A-1 Power relationships used in Simulations 1–4 42

Preface

A concise version citing this report was submitted to the *Journal of the Mechanical Behavior of Biomedical Materials*, and currently it is in the process of publishing.

Acknowledgments

The authors acknowledge many helpful discussions with their US Army Combat Capabilities Development Command (DEVCOM) Army Research Laboratory (ARL) experimental coworkers during this research: C Allan Gunnarsson, Dr Andrew Brown, and Dr Karin Rafaels. Without their unique experimental mechanics and biological material expertise, we would not have been able to execute our vision laid out at the beginning of this report. We also express our gratitude for the meshing assistance with corresponding elemental bone-volume fraction provided by Maya Choukair from Materialise USA LLC. We especially express our deep appreciation for the helpful suggestions provided by Dr Richard Becker of DEVCOM Army Research Laboratory whenever we encountered issues with Abaqus, thus allowing us to confidently design VUMAT and use the finite-element code, and for providing suggestions for modeling the response of failed material. Specifically, his suggestions regarding how to model the response of elements after failure, allowing us to continue the simulations after local failure up to the initiation of global catastrophic failure, thus enabled the critical comparison of the final simulated cracked skull structure with the corresponding 3-D failed structure from the experiment, showing remarkable similarity. We also thank our former Branch Chief of the Soldier Protection Sciences branch, Dr Chris Hoppel, for believing in us in our effort to validate the hybrid experimental-modeling-computational concepts we were articulating. In addition, we really appreciate Jessica Sun for scanning the pre- and post-loaded skullcaps using our North Star computational tomography capabilities at ARL's Weapons and Materials Research Directorate. Finally, we also acknowledge the contribution of Panagiotis (Pete) Saliaris, who helped identify the cracking patterns in the pre- and post-loaded skullcap microtomographs during his time in the laboratory as a summer intern.

Executive Summary

A comprehensive cellular or tissue-based capability to understand possible dominant injury mechanisms in the brain under multi-axial stress-states and rates is currently not available. In the meantime, skull fracture could serve as an indication of head injury. Therefore the ability to predict the initiation of skull fracture through finite-element (FE) simulation can serve as an in silico tool for assessing various head-protection scenarios for their level of effectiveness. For this objective, an iterative inverse FE methodology (inverse to the normal procedure of obtaining model parameters directly from experimental response) was recently developed to predict the initial linear response followed by the subsequent nonlinear mechanical response and the evolution of fracturing patterns of the human skull under uniaxial compression. The methodology was based on assuming that deviation from linear response was due to local elemental failure. Here, this concept was further extended to represent the multi-axial loading condition of the in vivo skull by considering possible different dominant failure-mechanisms of fracture during any low-rate impact event to the head while also incorporating the influence of the heterogeneous microstructural details. At the start of the inverse iterative procedure, element-specific initial material heterogeneity at each location of the skullcap was represented by calculating moduli and failure stresses from the local bone-volume-fraction of the element through power-law relationships. Initially, the values of these microstructure-dependent material parameters of the power laws were taken a priori from previous literature, derived for basic pure stress-states: uniaxial compression and tension, and simple shear. A microstructurally inspired mechanism-based failure surface was used for failure thresholds, representing fracture initiation from different dominant mechanisms of skull failure. The a priori values for the initiation thresholds of different failure mechanisms were iterated and optimized for the predicted load displacement to represent that of the corresponding indentation experiment on a 3-D skullcap specimen, specifically extracted so as to more closely preserve the in vivo multi-axial loading environment. Using the optimized values of the failure thresholds, each element was allowed to fail during the simulation in tension, compression, or shear, corresponding respectively to clinical linear, depressed, or penetrating shear-plug failure (fracture). Element-level failure enabled the visualization of the evolution of fracture by different mechanisms, starting from initiation to initial propagation, resulting in the final crack pattern at the time of macroscopic (clinically identifiable) injury. Before the appearance of the catastrophic unstable fast crack, the failed cracked structure predicted by the simulation represented remarkably well the crack pattern from the corresponding experiment, when

visualized through 3-D tomography, thus validating the implemented hybrid experimental-modeling-computational concept.

1. Introduction

A key concern for protecting a Soldier in theater is the extent of our ability to mitigate the risk of injuring the brain. Ideally, identification of conditions that induce brain injury, resulting in less than optimum short- and long-term injury outcomes, should be based on exceeding mechanical injury thresholds acting on the scale of cells and tissues in the brain, leading to structural and subsequent functional degradation. However, a definitive set of injury criteria at this scale based on strain-rate and multi-axial stress/strain-state remains elusive, and is currently not available. Meanwhile, if we can identify mechanical thresholds for skull fracture under a multi-axial state of stress, then those thresholds can serve as a more readily identifiable and clear indication that head injury has occurred. Therefore, the ability to predict the onset and location of various types of skull fracture in the battle theater for a multitude of different impact or blast scenarios, through modeling and simulation, can provide a valuable research tool for design of new and evaluation of existing head-protection systems.

However, predicting skull fracture is nontrivial due to the structural heterogeneity of the skull and complexities associated with the multi-axial stress-state and regimes of strain-rates of loading. In this study, we attempt to address microstructural heterogeneity and multi-axial loading at quasi-static rates. Figure 1 provides an overview of existing experimental studies on skull mechanics.

stress-state	Layer type Avg BVF	cranial bone-type	loading rate (1/s)	author	E or G (GPa)	failure stress (MPa)	emax	U kJ/m^3
compression DIC	mid-diploe (MD) BVF=0.457	frontal wet	0.001	Alexander et al BVFmodel	2.6 ±0.6	31.9 ±22.8		
compression DIC	MD BVF=0.371	parietal wet	0.001	Alexander et al BVFmodel	1.9 ±0.4			
compression DIC	outer-table (OT) BVF=0.945	frontal wet	0.001	Alexander et al BVFmodel	7.8±0.2	255.3 ±27.9		
compression DIC	OT BVF=0.904	parietal wet	0.001	Alexander et al BVFmodel	7.3 ±0.5			
compression DIC	inner-table (IT) BVF=0.838	frontal wet	0.001	Alexander et al BVFmodel	6.5 ±0.6	173.0 ±24.2		
compression DIC	IT BVF=0.841	parietal wet	0.001	Alexander et al BVFmodel	6.5 ±0.6			
compression DIC	composite BVF=0.688	frontal wet	0.001	Alexander et al BVFmodel	3.9 ±0.8	31.9 ±22.8		
compression DIC	composite BVF=0.542	parietal wet	0.001	Alexander et al BVFmodel	2.5 ±0.7			
compression	composite	frontal	0.001	Alexander et al platen measurements	2.5±1.4	31.9 ±22.8		
compression DIC	composite	frontal	0.001	Alexander et al average DIC-strain composite	4.0±2.0	31.9 ±22.8		
shear	OT BVF=0.922	wet	0.001* and 0.1*	Brown et al		88.3±9.0		
shear	IT BVF=0.879	wet	0.001* and 0.1*	Brown et al		73.2±11.2		
shear	MD BVF=0.517	wet	0.001* and 0.1*	Brown et al		19.7±3.4		
compression	composite	normal-E	QS	McElhaney et al	2.41	74		
compression	composite	tangential-E	QS	McElhaney et al	5.58	97		
torsion	diploe		QS	McElhaney et al	1.38	22		
direct shear	diploe		QS	McElhaney et al		21		
tension	composite	tangential-E	QS	McElhaney et al	5.38	43		
tension	table	tangential-E	QS	McElhaney et al	1.23	79		
tension 1.5mm thick Strain Gage	cortical from regress-line	frontal, parietal, temporal wet 25-95 yrs	0.005	Wood (1971)	11.55	48	0.0072	294
			1		15.98	83	0.0063	
			150		20.18	127	0.0051	
bend-tension	composite		QS	Hubbard (1971)	9.50	-		
bend-tension computed	IT-inner_surface	frontal-W	21.77±5.69** (0.5m/s)	Motherway et al	4.85 ±1.71	90.80 ±13.34		183±48
bend-tension computed	IT-inner_surface	parietal-W	20.97±7.53** (0.5m/s)	Motherway et al	8.02 ±2	83.4 ±26.85		107±50
bend-tension computed	IT-inner_surface	frontal-W	26.28±6.64** (1m/s)	Motherway et al	4.87 ±1.93	102.60 ±36.20		193±91
bend-tension computed	IT-inner_surface	parietal-W	28.42±8.26** (1m/s)	Motherway et al	13.57 ±9.68	80.57 ±21.89		88±43
bend-tension computed	IT-inner_surface	frontal-W	103.98±18.85** (2.5m/s)	Motherway et al	16.34 ±10.18	126.91 ±48.76		139±43
bend-tension computed	IT-inner_surface	parietal-W	108.07±29.16** (2.5m/s)	Motherway et al	15.46 ±9.93	128.37 ±49.28		176±11
compression	composite-E			Robbins and Wood	1.39	36.54		
simple-shear	diploe-E			Robbins and Wood		13.10		
compression	diploe			Melvin (1969)	1.03	32.4		
Tension-DIC	OT-derived BVF=0.928	combined-W	QS	Boruah et al UVA (2017)-BVFmodel	15.8	88.9		
Tension-DIC	MD-derived BVF=0.420	combined-W	QS	Boruah et al UVA (2017)-BVFmodel	2.7	9.7		
Tension-DIC	IT-derived BVF=0.839	combined-W	QS	Boruah et al UVA (2017)-BVFmodel	12.6	67.1		

Fig. 1 Overview of previous experimental mechanical characterization of the human skull. Authors include Alexander et al. (2019, 2020a), Brown et al.* (2020), McElhaney et al. (1970), Motherway et al. (2009), and Robbins and Wood (1969). Asterisk (*) indicates the reported strain rates were obtained from displacement rate of the shearing punch divided by the gage length of the total specimen in the loading direction. Double asterisk (**) indicates that the method of obtaining these reported constant strain rates was not defined.**

The large variation in modulus and failure stress values illustrates the difficulties in characterizing the mechanical response of the skull, generally, and skull failure, specifically. One difficulty is the challenging heterogeneous structure of the skull, which can be described as a three-layered sandwich structure. The outer table nearest to the outer skin and the inner table nearest to the brain are composed of relatively dense cortical bone with average porosities of roughly 7% and 16%, respectively (Alexander et al. 2019). The outer and inner layers surround the highly porous diploë, where the porosity can spike to more than 80%. The porosity gradient has significant mechanical implications because both the modulus and yield strength of bone are known to vary exponentially with the bone volume fraction (BVF), which is defined as 1 minus the porosity (readers are referred to reviews by Gibson and Ashby [1997] and Morgan et al. [2018]). The modulus (Young's modulus, E) and strength (maximum/minimum principal or maximum shear stress, σ_f) are commonly related to the BVF or a correlative measure, such as the apparent density, by power relationships. For the case of using BVF (f_{BV}), these relationships are of the form

$$E = E_0 \cdot (f_{BV})^k \tag{1}$$

$$\sigma_f = \sigma_{f,0} \cdot (f_{BV})^m \tag{2}$$

The leading coefficients represent the modulus (E_0) and strength ($\sigma_{f,0}$) of solid bone tissue material, for which there is no porosity (f_{BV}=1), and also a function of nonstructural measures such as bone chemistry, which is a function of the age, species, nutrition, and the environment. These parameters for the modulus and strength of the solid bone material are then scaled by the BVF raised to the exponent (k or m), respectively. Reviews of experiments on different types of bone have indicated that the exponent factor for modulus falls between k = 1~3, while the factor for both compressive and tensile strength is on average m = 2 (Gibson and Ashby 1997; Morgan et al. 2018), thus underlining the significance of the large porosity (microstructural) variation within the skull on its mechanical response.

Accurately modeling the porosity gradient of the skull is particularly challenging in finite-element (FE) simulations. Some FE models of the head do not mesh the skull-bone microstructure at the length scale of the pores in the diploë and tables. Instead, the boundaries of the skull mesh are identified from the rough shape of the outer and inner surfaces, and the skull is modeled as a homogeneous material (e.g., Tse et al. 2014). A limitation of this homogeneous method is that it fails to capture the large gradient in porosity, which likely has a significant role in the mechanical response of the skull, particularly in failure. One method to account for the porosity

gradient has been to model the skull as a three-layer system (e.g., Deck and Willinger 2008; Cotton et al. 2016; Lozano-Minguez et al. 2018; Ptak et al. 2018; Alexander and Weerasooriya 2020). However, this method models the diploë as a homogenous material, whereas the porosity has been shown to vary greatly even within the diploë, since the porosity variation from the outer to the inner surface of the skull can be well-described by the bell-shaped Gaussian function (Alexander et al. 2019).

Another method to more closely capture the biological porosity distribution, while avoiding to explicitly mesh the bone microstructure, starts with a volume filled with elements, as in the homogeneous method. It then assigns each element a BVF value, or correlative measure such as apparent density, by mapping the element to the micro-computed tomography (CT) images. The BVF or density of the element is then used to assign microstructure-dependent mechanical properties to each element. Therefore, the mechanical properties can vary among the elements throughout the mesh based on the local microstructure of the volume within the actual physical specimen, which the element is meant to represent. This type of variation is referred to here as element-BVF-specific. The corresponding method, referred to herein as the elemental method, has been successfully used to model various bones including femur (Bessho et al. 2007; Taddei et al. 2007; Helgason et al. 2014), shoulder (Knowles et al. 2019), and vertebrae (Robson Brown et al. 2014). The key advantage of this method is that each element can then be assigned mechanical properties based on the local averaged BVF of the element, relying on relationships between BVF and mechanical properties in the form of Eqs. 1 and 2, thus significantly reducing the computational cost as well as increasing the ability to solve existing practical problems in reasonable time frame.

Only a few recent studies have started to use this elemental method in modeling the skull. For example, Haen et al. (2018) assigned microstructure-dependent moduli to elements of a human skull mesh using a modulus-density relationship derived from experiments on human femurs (Zannoni et al. 1999). In addition, both Chamrad et al. (2018) and Motherway (2012) implemented element-varying moduli in their FE models of the human skull using a modulus-density relationship previously published (Carter and Hayes 1977), which had been derived from experiments on human and bovine femurs and tibia. However, femur deformation and fracture response is orientation- and rate-dependent (Shannahan et al. 2015; Sanborn et al. 2016; Weerasooriya et al. 2016), and the fact that this relationship was not optimized specifically for the skull was noted as a limitation by authors. However, a few researchers recently reported modulus-BVF and failure-stress-BVF power relationships derived specifically for fresh human skull specimens under uniaxial compressive (Alexander et al. 2020a), tensile (Boruah et al. 2017),

and shear loading (Brown et al. 2020). Based on these skull-specific relationships, Alexander and Weerasooriya (2020a) implemented element-BVF-specific, microstructure-dependent mechanical properties in an FE model of quasi-static compression of a coupon-sized human skull specimen.

The present study applies the elemental method to model the quasi-static indentation of a skullcap specimen (3-D beam) extracted from the human skull. It extends our previous work on modeling uniaxial compression by using a specimen geometry closer to the in vivo skull, applying external loading more representative of in situ forces, and adding the shear mechanism of failure. The details of the specimen extraction and indentation experiment were reported by Gunnarsson et al. (2019). A few prior studies had reported the mechanical response of human skull specimens to compression, but the specimens were in the form of small circular or square coupons (Robbins and Wood 1969; McElhaney et al. 1970; Boruah et al. 2013; Alexander et al. 2020a) or 2-D beam strips, where the out-of-plane dimension was relatively small (e.g., Hubbard 1971; Motherway et al. 2009; Auperrin et al. 2014; Shannahan et al. 2015; Sanborn et al. 2016). On the contrary, the geometry of the "skullcap" specimen was purposely chosen to more closely mimic the 3-D in vivo loading configuration of the skull and to be able to measure full-field backface (inner surface) deformation resulting from loading applied to the outer surface, which is not possible with the full skull. Assessing the backface deformation and failure, a key to determining the severity of conditions causing brain injury, would not be meaningful using the previous coupon and beam strip geometries.

The skullcap under experimental uniaxial compression showed an initial linear load-displacement response, followed by softening until ultimately reaching failure. Here, the apparent nonlinearity after initial linear response of the specimen at the global level is modeled through localized failure at the element level, assuming the deviation from linearity is due to failure at local scale. The ability of implementing element-BVF-specific, microstructure-dependent failure criteria in order to effectively model macroscopic nonlinearity in the force-displacement response has been successfully demonstrated previously for other bones such as the femur (e.g., Bessho et al. 2007; Hambli 2013, Enns-Bray et al. 2018) and more recently for the case of skull coupons (Alexander and Weerasooriya 2020a). In the present skullcap simulation, the elements were assumed to fail either by compression, tension, or shear corresponding to clinical linear, depressed, and penetrating shear-plug macro failure, respectively. Failure was determined by monitoring the stress-state of the element and comparing it to BVF-dependent (microstructure-inspired) failure criteria specified for each mechanism (compression, tension, or shear). The majority of studies, which reported power

relationships between BVF and mechanical properties were derived for bones at anatomical locations other than the skull. However, a few studies have directly used skull bone to derive power relationships between the BVF and the modulus (Boruah et al. 2017; Alexander et al. 2020a; Brown et al. 2020), compressive failure stress (Alexander et al. 2020a), tensile failure stress (Boruah et al. 2017), and shear failure stress (Brown et al. 2020). These relationships were used as starting points to iteratively determine optimal parameters for the BVF-dependent failure criteria for different stress-states.

2. Methods

2.1 Specimen Extraction and Quasi-Static Indentation Experiment

The experiment documented here was conducted in compliance with the US Army Combat Capabilities Development Command (DEVCOM) Army Research Laboratory (ARL) Policy for Use of Human Cadavers for Research, Development, Test, and Evaluation under the guidance and oversight of the DEVCOM Army Research Laboratory Human Cadaver Review Board and the ARL Safety Office. The experiment was part of a larger study on the mechanical response of human skull to indentation loading. Only a basic outline is provided here; the reader is referred to the experimental study Gunnarsson et al. (2019) for complete details. Briefly, a skullcap specimen was extracted from the right parietal bone of a postmortem human subject (73-year-old male, 68 kg at death, with internal label of ARL-2017-0016-RPAR) using a pathology bone saw (EXAKT 312, EXAKT Technologies, Inc.). Figure 2 details the 3-D geometry and curvature of the specimen. The different physical sides of the specimen will be referred to in this report with the following terms: anterior (toward the front of the donor), posterior (toward the rear of the donor), superior (toward the top of the head), and inferior (toward the shoulders.) The dimension spanning the thickness from the inner surface (nearest to the brain) to the outer surface (nearest to the outer skin) is referred to as the through-thickness dimension.

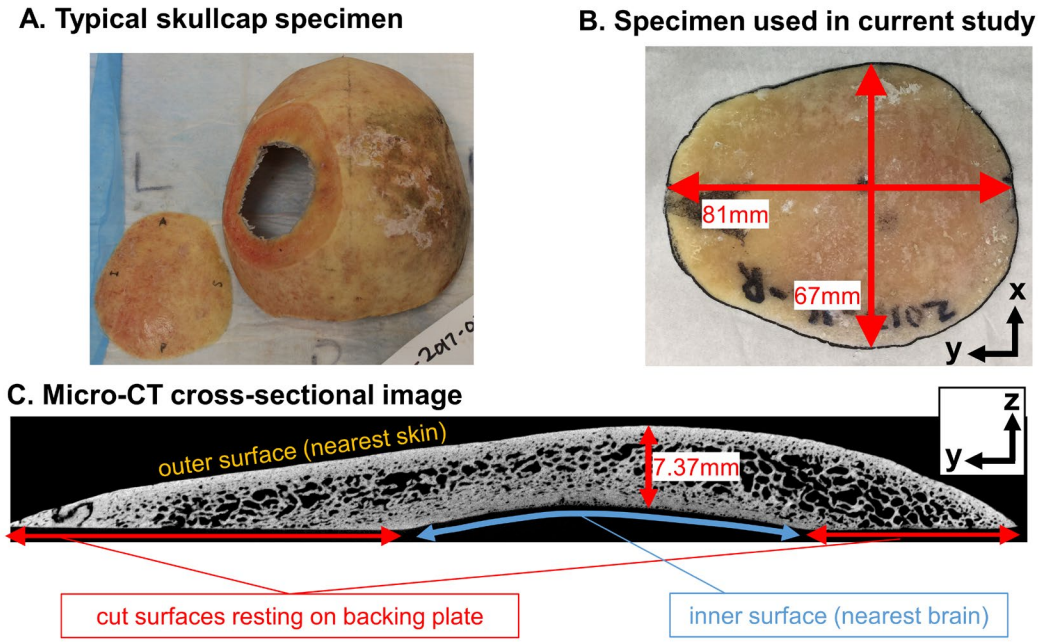

Fig. 2 Skullcap specimen: A) example of a typical skullcap specimen after extraction from the top part of the skull, B) top-down view of the skullcap specimen used in the current study, showing the outer surface (nearest to the skin), and C) cross-sectional micro-CT image of the skullcap specimen, with gray representing bone and black representing pores or the surrounding medium

The microstructure of the specimen was characterized and quantified using high-resolution micro-CT with an isotropic voxel size of 27 μm^3 (Northstar XRD 1620). After scanning, the skullcap was loaded using an indentation loading method at a quasi-static rate. Indentation was generated via load frame (Instron 8871) with a steel indenter with a hemispherical tip (diameter = 31.75 mm) attached to the crosshead. The point of contact between the indenter and the specimen (point of indentation/impact, POI) was on the outer surface of the skullcap approximately at its apex. The indenter moved into the specimen, in the through-thickness direction, at a constant rate of 0.005 mm/s. The specimen was supported by an aluminum backing plate and rested freely on the plate, unconstrained in the plane of the plate. The plate had a custom-shaped viewing port at the center through which cameras were used to record the 3-D surface deformation of the skull inner surface (backsurface) while the outer surface was indented. The specimen was aligned on the plate such that the POI was approximately over the center of the viewing port. Load on the skull specimen was measured using a traditional load cell (Instron, capacity 5 kN) connected to the indenter. After loading, the skull specimen was scanned with the micro-CT to obtain quantitative data on fracture and damage caused to the structure, with pre-test and post-test images co-registered using DataViewer software (Bruker microCT).

2.2 Microstructurally Inspired and Mechanism-Based (MIMB) Model of Failure in the Human Skull

In this section, the proposed concept for modeling failure (or fracture) of the human skull is presented. Implementation of this concept in FE simulations is described in Section 2.3.

2.2.1 Dominant Mechanisms of Initiation of Skull Failure during Indent Loading

Different fracture modes and the effect of the impactor shapes that will promote these different fracture modes are identified in Fig. 3. Here, major skull fractures (failure) are assumed to be clinically identifiable by three different dominant mechanisms: linear fracture, depressed fracture, and penetration failure. Final mixed fracture could be a combination of these three mechanisms, but initiation of the failure is probably dominated by one of these modes of failure based on the stress-state. For example, linear fracture occurs due to bending of the skull, and failure most probably initiates at the surface of the inner table (nearest to the brain) due to tensile deformation. On the other hand, depressed fracture is dominated by compressive loading, and mostly initiates in the diploë region with low BVF due to the buckling of the walls of the pores in this region. Penetration or plugging failure is dominant when impactor penetrates the skull by shear.

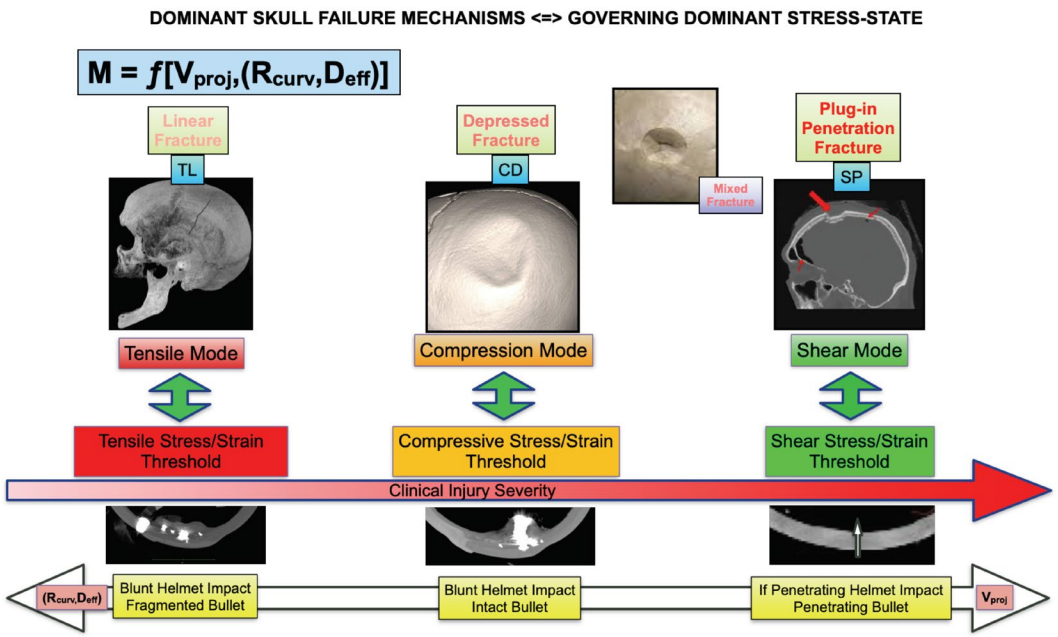

Fig. 3 The three dominant initiation mechanisms of skull failure—linear fracture, depressed fracture, and shear plug fracture—are represented together with their correlated stress thresholds: tensile, compressive, and shear, respectively. Subsequent failure after initiation could be mixed-fracture of these dominant mechanisms. The specific mechanism (M) by which the skull fails in a given loading condition is assumed to be a function of the velocity (V_{proj}) and geometry of the projectile, specifically its radius of curvature (R_{curv}) and effective diameter (D_{eff}). (Unpublished skull and helmet pictures courtesy of Karin Rafaels, ARL; depressed and mixed fracture pictures are public domain from the National Institutes of Health [NIH])

Of these three failure mechanisms (tensile, compressive, and shear), the specific one by which a region of the skull fails during a given impact event depends on the velocity and the shape or geometry of the indenter/impactor (Fig. 3). Moreover, the impactor geometry and velocity is also assumed to be predictive of the clinical injury severity, with the severity inversely proportional to the radius of curvature and directly proportional to the velocity (DiMaio 1999). For example, in the least-severe cases when the surface of the impactor has a large radius of curvature or effective diameter, the impact event will promote bending of the skull leading to tensile dominant linear fracture (noted as TL in Fig. 3). A fragmenting bullet impacting a barrier such as a helmet can promote this scenario. For these cases, the maximum tensile stress calculated from the stress-state in the impact zone of the skull would likely reach its tensile failure threshold sooner than would either the maximum compressive stress or maximum shear stress reach their respective thresholds. On the other extreme, if the impacting surface has a very small radius of curvature (i.e., the impactor is sharp-tipped), the impacting surface could penetrate the skull, leading to a shear plugging type of skull failure (noted as SP in Fig. 3). This most clinically severe scenario is equivalent to when a sharper

nonfragmenting bullet penetrates a protecting helmet or barrier. For these cases, the maximum shear in the impact zone would reach its threshold sooner than would the maximum tensile or compressive stresses reach their respective thresholds. Finally, if the bullet is neither fully fragmenting nor penetrating, the impacting surface could compress the low-BVF diploë region, leading to the initiation of the depressed failure in some regions of the skull, before shearing and tensile fracture discussed earlier. The compressive failure threshold dominates this type of failure initiation, noted as CD in Fig. 3.

Based on these proposed concepts, Fig. 4 shows the failure mechanism map for skull bone in the maximum-principle and maximum-shear stress plane for quasi-static rate of loading, with corresponding failure modes. In this stress plane, a rectangular failure locus is assumed: the right-hand border of the rectangle is specified by the tensile failure threshold, the left-hand border by the compressive threshold, and the top and bottom borders by the shear threshold. However, stress-states near the corners of the rectangle could induce mixed modes of competing failure with no dominant mechanism of failure initiation, and thus the true failure surface may deviate from the proposed idealized rectangular failure locus near the corners. More-detailed combined experimental-computation studies in future can refine the proposed mechanism-based failure surface.

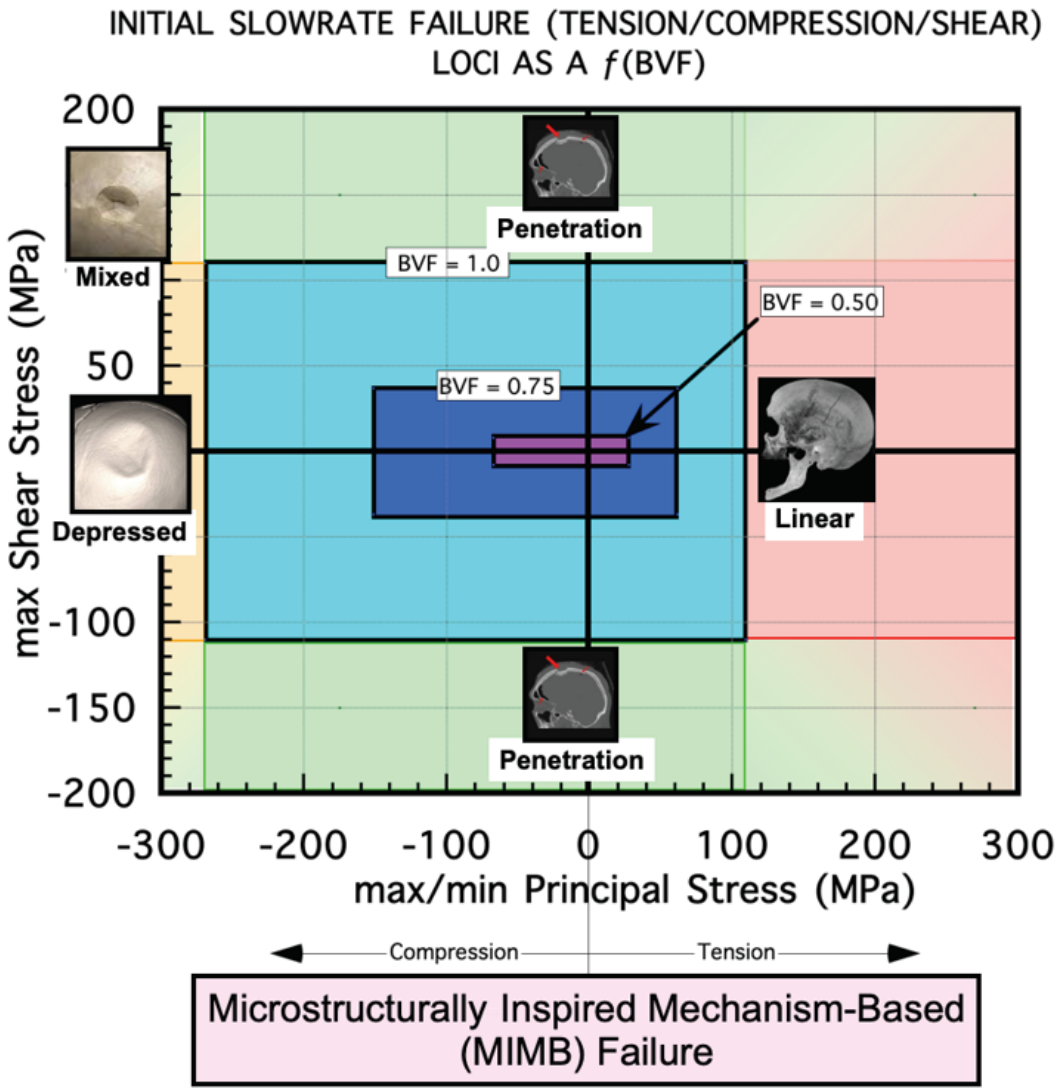

Fig. 4 Proposed failure mechanism map for human skull shown in the plane of principal stress and max shear-stress (unpublished pictures of fractured skulls courtesy of Karin Rafaels, ARL; depressed and mixed fracture pictures are public domain from the NIH). A rectangle failure surface is purposed: the skull is predicted to fail if the stress-state falls outside the rectangle, but does not fail if it remains within the rectangle. Failure by linear fracture is assumed when the maximum principal stress exceeds its threshold (right-hand bounds of the rectangle), in depressed fracture when the magnitude of the minimum principal stress exceeds its threshold (left-hand bounds of the rectangle), and by shear plug penetration when the magnitude of the maximum shear stress exceeds its threshold (top and bottom bounds of the rectangle). The thresholds are microstructure-dependent, calculated from the BVF by power-laws. Three examples are shown for BVF values of BVF = 0.50 (inner purple rectangle), BVF = 0.75 (dark blue), and BVF = 1.0 solid bone (light blue). The thresholds for these BVF examples were calculated using relationships previously published from experiments on human skull coupons (Boruah et al. 2017, Alexander et al. 2020a, Brown et al. 2020).

2.2.2 Microstructurally Inspired

According to the concept of skull failure mechanisms just presented, the stress-state of the skull during an impact event can vary from one location of the skull to another, such that there exist fields of max-shear and max-principle stresses. These regional variations cause failure to initiate by different mechanisms in different parts of the skull. At the same time, the microstructure of the skull also varies from location to location, further complicating the derivation of stress-state (hence dominant mechanism)-dependent failure criteria. However, Boruah et al. (2017), Alexander et al. (2020a), and Brown et al. (2020) have experimentally investigated the initiation of failure in the human skull using systematic experiments under quasi-static rates for uniaxial compressive, tensile, and simple shear loading, respectively. These researchers found that the failure thresholds in compression, tension, and shear can be related via power-law relationships to details of the microstructure, as represented by the variable BVF. The state variable or the leading coefficient (also the solid bone strengths) of each power law represents the bone chemistry, which is a function of the age, species, diet, environment, and remodeling of the bone. Figure 4 shows the initial failure MIMB failure maps for skull bone, based on the data in the literature (Fig. 1).

2.3 Finite-Element Simulation

FE simulations were completed using Abaqus Explicit. Figure 5 shows the FE model. The coordinate system was defined with the indenter motion in the z-dimension and the backing plate in the x-y plane. The backing plate with viewing port was meshed as three elements thick (Fig. 5A) using reduced-order eight-node brick elements (C3D8R). The plate was assigned elastic material properties for aluminum: E = 69 GPa, ν = 0.35, and ρ = 2.72 g/cm^3, where E, ν, and ρ are the Young's modulus, Poisson's ratio, and mass density, respectively. Plate displacement in all three directions was constrained at four locations near the corners of the plate, modeling the experimental setup where the plate was supported by four through-thickness bolts near the corners.

The indenter was modeled as a rigid solid. The indenter was constrained in all degrees of freedom apart from displacement in the z-direction, u_z, which was specified to increase from $u_z = 0$ to $u_z = \delta_{max}^{top}$ in 10 ms. The maximum vertical displacement of the indenter, δ_{max}^{top}, was specified as 3.3 mm, which corresponded to roughly 3 mm of indentation into the specimen after accounting for a small standoff distance. The Abaqus formulation for hard general contact was specified between the indenter, specimen, and backing plate, with a friction coefficient of 0.1. No other boundary conditions were specified for the specimen.

The skullcap was meshed using approximately 230,000 four-noded, first-order tetrahedral elements (C3D4). The mesh was generated from the micro-CT imageset using the Mimics Innovation Suite (MIS, Materialise USA LLC, Plymouth, Michigan). The average BVF of the physical volume that each element represented, rounded to the nearest 0.01, was also calculated using MIS. This value of BVF was used as the BVF of the element at the start of the simulation, $f_{BV,0}$, in order to calculate BVF-dependent material properties, as detailed below. The skullcap mesh is shown in Fig. 5, where the BVF distribution is compared with the micro-CT images (Fig. 5c). As seen in Fig. 5, the mesh was more highly refined in the central region under the POI, transitioning to a coarser refinement at the periphery.

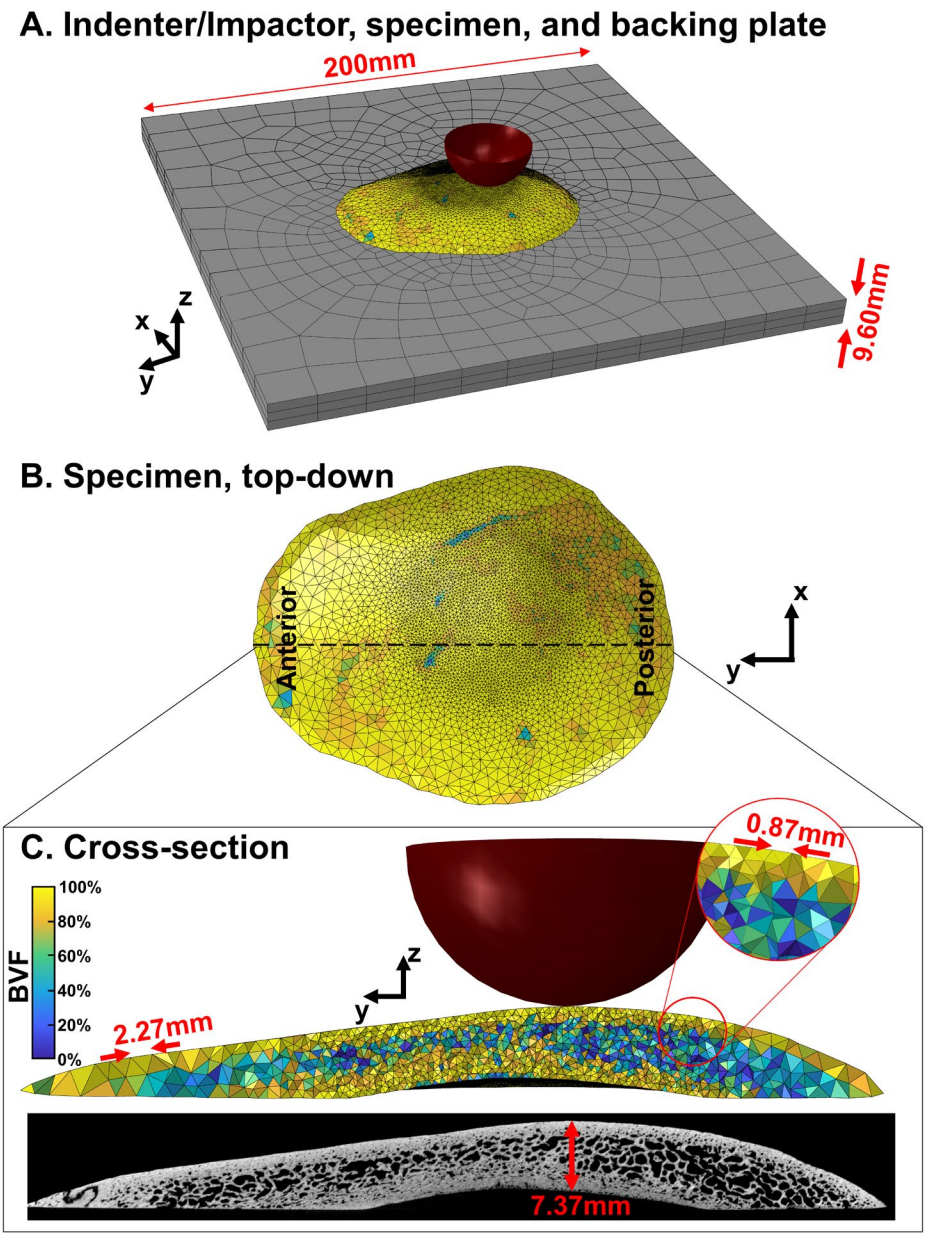

Fig. 5 Skullcap simulation geometry. A) skullcap resting on the backing plate, together with the indenter/impactor at the POI. B) Top-down view of the specimen, where the gradient in element sizes is clearly visible from largest at the perimeter to smallest under the POI. (C) Anterior–posterior cross section of the specimen under the POI. In all subfigures, the elements of the specimen are color-coded by BVF, as indicated in the color bar in (C). Indenter/impactor diameter was 31.75 mm. Maximum transverse dimensions of skullcap: y = 88.86 mm and x = 71.97 mm.

Material properties were assigned to the elements based on $f_{BV,0}$. The stress for each element at a given increment (time point), $t = i$, was calculated using a custom-written (vectorized) user-specified material subroutine (VUMAT). The VUMAT procedure is depicted in the flowchart of Fig. 6. The VUMAT subroutine

of Abaqus allows the user to directly calculate the stress of each element based on a custom procedure and the current state of the simulation. Here, current values of variables at $t = i$ will be referred to with the subscript i. The original value of variables at the start of the simulation ($t = 0$) will be referred to with the subscript 0. At the start of the simulation, all elements had a linear elastic response, with a Poisson's ratio of $\nu = 0.3$ and a Young's modulus (E, in gigapascals) given by a power relationship based on the original BVF at the start of the simulation (Eq.1). The parameters of this relationship were iterated to match the initial linear portion of the experimental load-displacement response, as presented in the Results section. The Poisson's ratio was assumed as a constant in this study. The possibility of this ratio varying with BVF is further elaborated in the Discussion section.

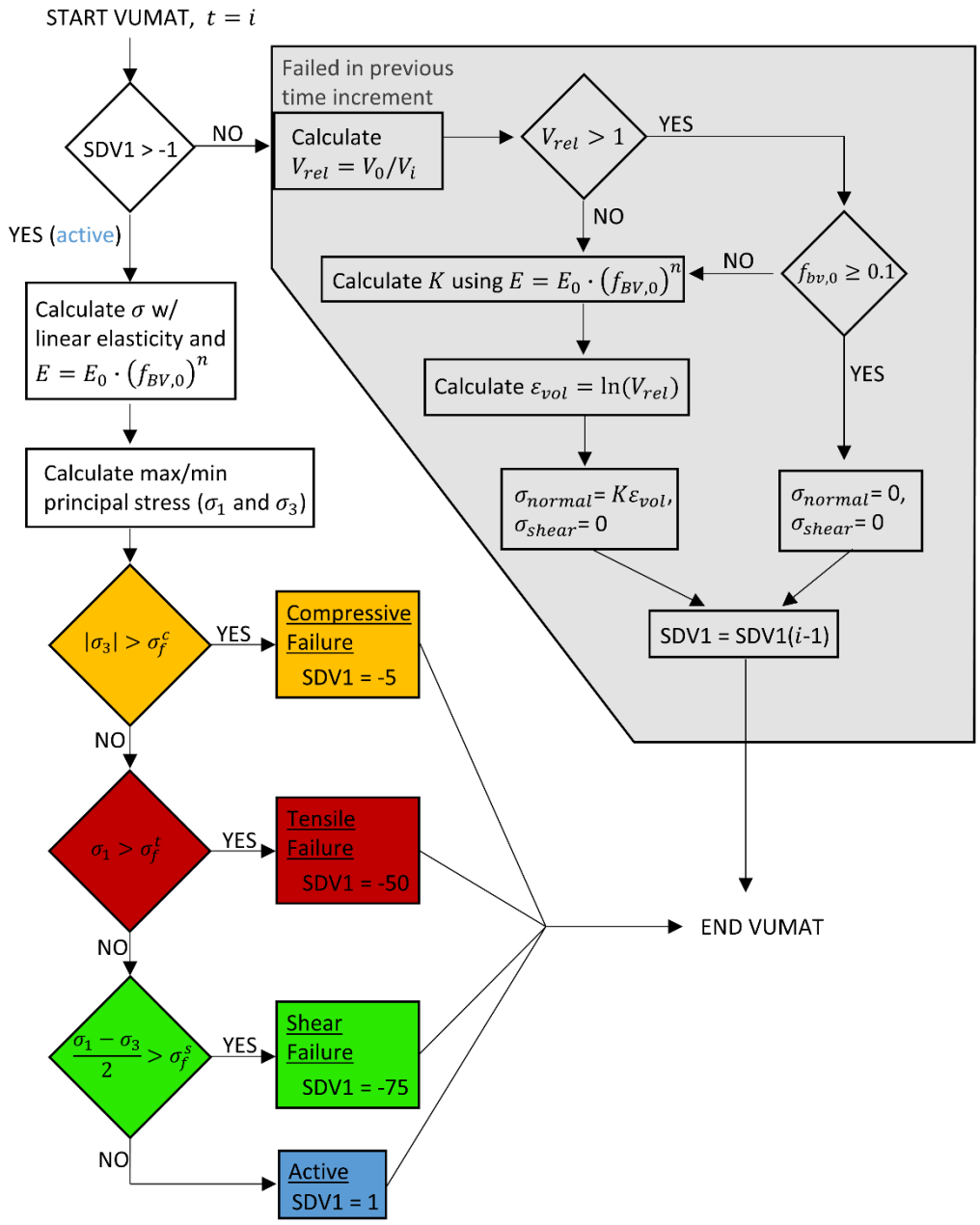

Fig. 6 VUMAT flowchart showing process for calculating the stress for a given element at the timepoint t = i. Element status is tracked via a state-dependent variable, abbreviated here as SDV1.

The density of each element was calculated by scaling the density of pure bone ($\rho_{b,0}$, for which f_{BV} was 1) by the BVF of the element:

$$\rho_0 = \rho_{b,0} \cdot (f_{BV,0}) \quad (1)$$

The density of pure bone was assumed to be $\rho_{b,0} = 1.8$ g/cm^3 (Mow and Huiskes 2005). Elements were also assigned criteria for failure in compression (σ_f^c), tension

(σ_f^t), and shear (σ_f^s). These failure criteria were in the form of power relationships as introduced by the functional form of Eq. 2, and were specified as

$$\sigma_f^c = \sigma_{f,0}^c \cdot \left(f_{BV,0}\right)^n \tag{2}$$

$$\sigma_f^t = \sigma_{f,0}^t \cdot \left(f_{BV,0}\right)^k \tag{3}$$

$$\sigma_f^s = \sigma_{f,0}^s \cdot \left(f_{BV,0}\right)^m \tag{4}$$

There were six parameters governing the three failure stresses of Eqs. 4–6: a leading coefficient and an exponent scaling factor for each. These parameters were iterated to identify the set of values for which the numerical load-displacement curve most closely matched the experimental curves, as presented in the Results section.

2.3.1.1 Active (Not Failed) Elements

All elements were active (not failed) at the start of the simulation. The current status of an element was tracked by a state-dependent variable (SDV1), where SDV1 = 1 denoted that the element was active. For any element that was active at the start of the given time point $t = i$, the stress of the element was calculated using linear elasticity. Then, the maximum and minimum principal stresses of the element, σ_1 and σ_3, were calculated to determine if the element failed as a result of the additional stresses accrued during the current time step. The element was considered to have failed if any of the following conditions were satisfied:

$$abs(\sigma_3) > \sigma_f^c \tag{5}$$

$$\sigma_1 > \sigma_f^t \tag{6}$$

$$\frac{\sigma_1 - \sigma_3}{2} > \sigma_f^s \tag{7}$$

Equations 7–9 represent failure occurring by compression, tension, and shear, respectively. If the stresses of an element met one of these criteria, the SDV1 value of the element was changed to a negative number (Fig. 6), thereby causing the element to be treated in the next time point ($t = i+1$) as a failed element. Otherwise, if the stresses of an element did not meet any of the failure criteria, the SDV1 value was again set to 1, and the element continued to be treated as active during $t = i+1$.

2.3.1.2 Failed Elements

Elements, which had failed in a previous time step, were treated as quasi-fluid materials (right-hand, shaded branch of Fig. 6). With few exceptions, failed elements generally only carried stress if they were in a state of compression.

Whether the element was in a state of compression was determined from the relative volume of the element, V_{rel}, by the following procedure. First, V_{rel} was calculated as the ratio of the original density of the element (Eq. 3) to the current density of the element:

$$V_{rel} = \rho_0/\rho_i = V_i/V_0 \tag{8}$$

In Eq. 10, the last expression is the ratio of the current volume of the element to its original volume. This volume ratio is equivalent to ρ_0/ρ_i due to the conservation of mass within each element ($m_i = m_0$). Therefore, the failed element was considered to be in a state of compression ($V_i \leq V_0$) if the following criterion was met:

$$V_{rel} \leq 1 \tag{9}$$

If Eq. 11 was satisfied, the failed element was treated as load-bearing. The volumetric strain ε_{vol} was calculated as

$$\varepsilon_{vol} = \ln(V_{rel}) \tag{10}$$

The stress-state for the failed element in compression was then calculated from the bulk modulus (K) of the element as

$$\begin{gathered} \sigma_{normal} = K\varepsilon_{vol} \\ \sigma_{shear} = 0 \end{gathered} \tag{11}$$

In Eq. 13, the bulk modulus was calculated from the original elastic modulus of the element (Eq. 1) and the Poisson's ratio:

$$K = \frac{E}{3(1-2\nu)} \tag{12}$$

However, if Eq. 11 was not satisfied ($V_i > V_0$), the failed element was considered to be in a state of tension. The treatment for such an element depended on its original BVF. If $f_{BV,0} \geq 0.1$, the element did not carry any stress for $t = i$. If $f_{BV,0} < 0.1$, the element was approximated as carrying stress, as determined by Eqs. 12–14. This later approximation of considering as loadbearing those elements with low BVF values, which had previously failed and were subsequently in tension, was a numerical device used to mitigate these elements from becoming severely distorted. This approximation did not noticeably affect the stress-strain response when used with simulations of human skull bone coupons (Alexander and Weerasooriya 2020a).

3. Results

The experimental and numerical load-displacement response is shown in Fig. 7, where the displacement was measured as the amount of indentation applied to the skullcap at the POI. The load in the experiments was measured from the load cell attached to the indenter. In the experiment, the skullcap catastrophically failed (indicated by the significant drop in load) macroscopically at an applied indentation of u_y = 2.37 mm, corresponding to the peak of the experimental load-displacement curve. This macroscopic failure point occurred when the specimen ruptured, defined here as the catastrophic event of a crack traversing the entire thickness of the skull from the inner to the outer table. Specimen rupture was accompanied by an acoustic emission, and the resulting macroscopic through-thickness crack was visible without the aid of micro-CT.

The parameters of the power relationships relating the BVF of the element to the element-specific modulus (Eq. 1) and failure strengths (Eqs. 4–6) were iterated by comparing the numerical and experimental load-displacement response of the skullcap. Initial values for parameters (E, $\sigma_{f,0}^{c}, \sigma_{f,0}^{t}, \sigma_{f,0}^{s}$) were obtained from literature as discussed earlier (Alexander et al. 2020a; Boruah et al. 2017; and Brown et al. 2020, respectively). Figure 7 provides a summary of the effect of the parameters on the load-displacement response of the simulation as compared with the experimentally measured response. The load in the simulations was measured as the reaction force of the rigid indenter in the z-direction, R_z. To give a summary of how response varies with different parameters, Fig. 7 shows the load-displacement response for four example simulations (of many) with different power-law parameters (Simulations 1–4). More details on the iterative procedure used to identify the power-law parameters inversely from experiments are presented in Appendix A.

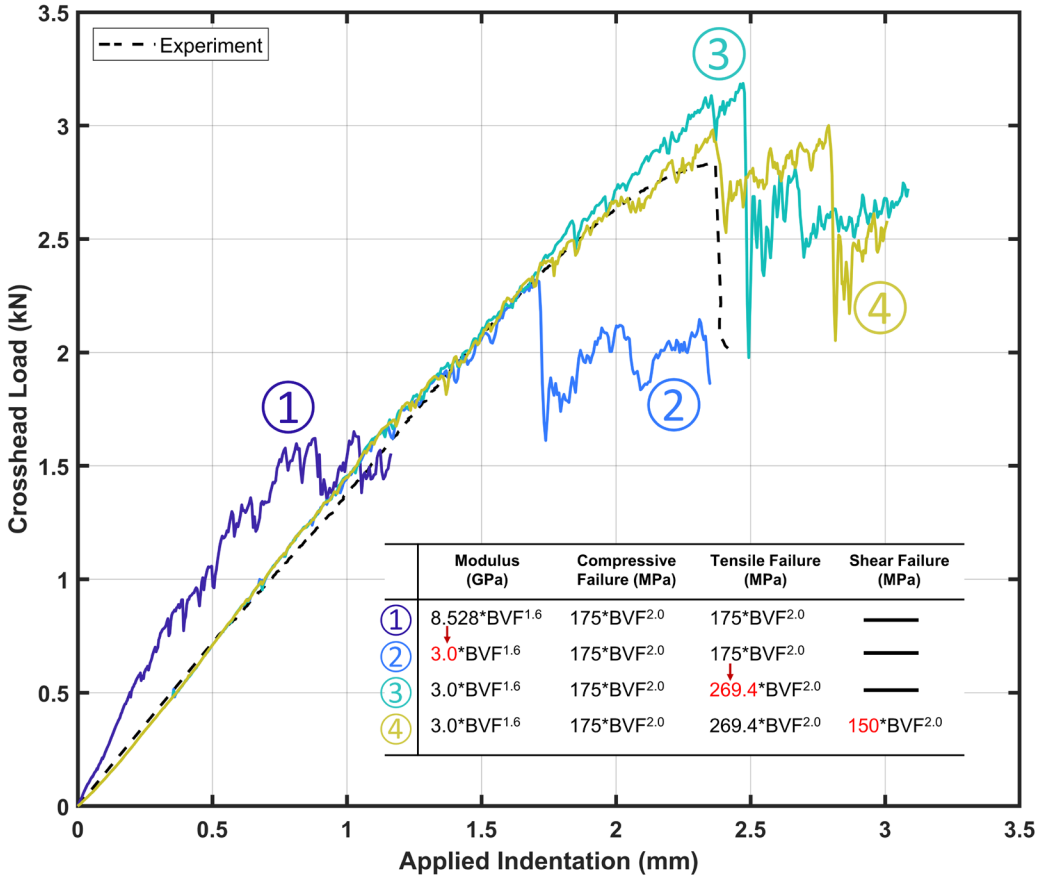

Fig. 7 Effect of power-law coefficients on the load-displacement response of the skullcap simulation as compared with the experiment. Displacement is measured as the amount of indentation ("applied indentation") of the indenter into the specimen. The crosshead load is measured directly from the test machine in the experiments. The load in the simulations is measured as the reaction force of the indenter in the indentation direction. The final optimized parameter values were used in Simulation 4.

The final parameter values were used in Simulation 4. Figure 8 shows the failure mechanism map for human skull, with the initial failure criteria (as in Fig. 4) and the final failure criteria, which were used in Simulation 4. Figure 9 shows the evolution of the number of elements, which failed by each of the three modes (tension, compression, and shear) during Simulation 4. Figures 10 and 11 compare the crack locations within the skullcap at the end of Simulation 4 with the crack locations in the experiment. The crack patterns in the experiment are highlighted by contrasting the micro-tomographs taken before and after the experiment. The simulated cracking pattern is illustrated by color-coding the elements based on their active/failed status.

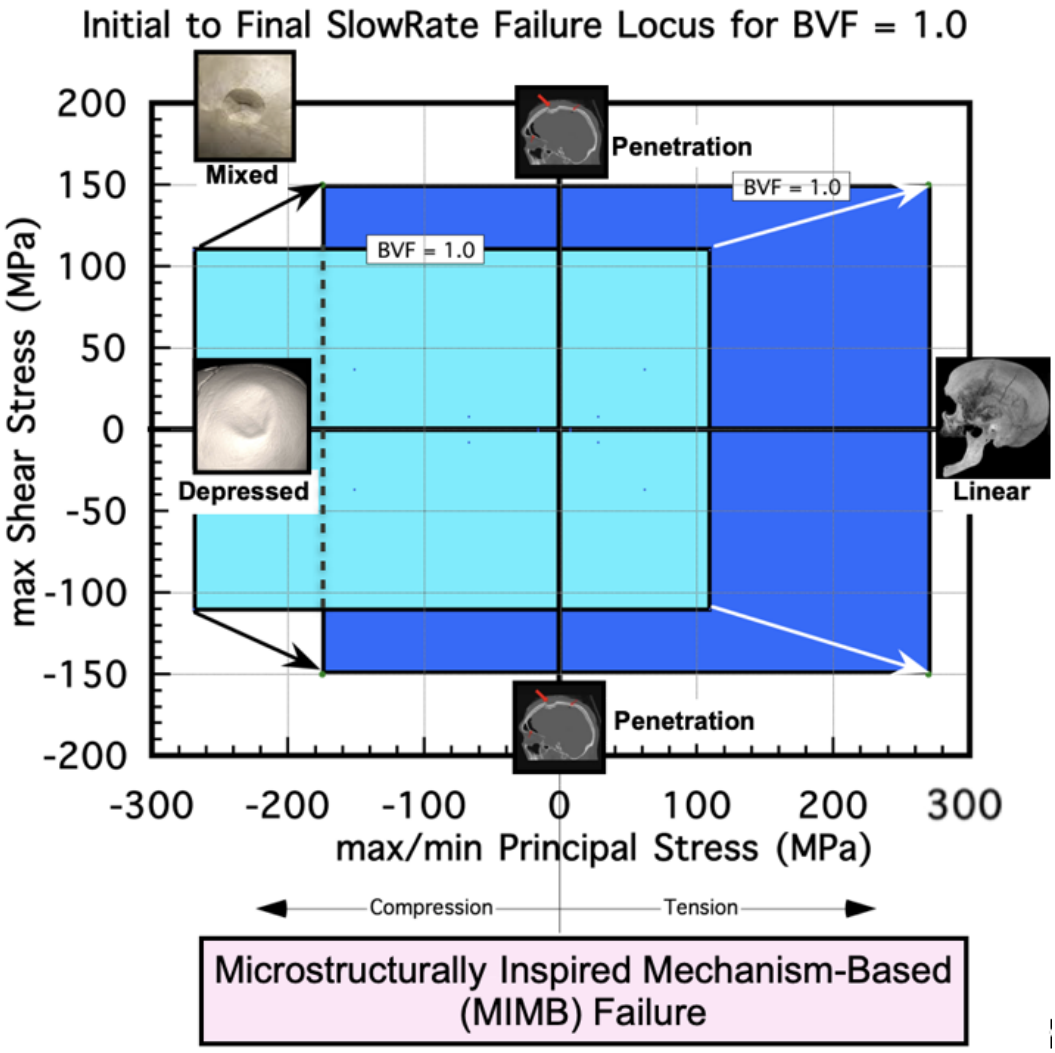

Fig. 8 Failure mechanism map, comparing the failure locus from initial values for the thresholds (light green rectangle, as in Fig. 4) with the final values used in Simulation 4 (dark green rectangle)

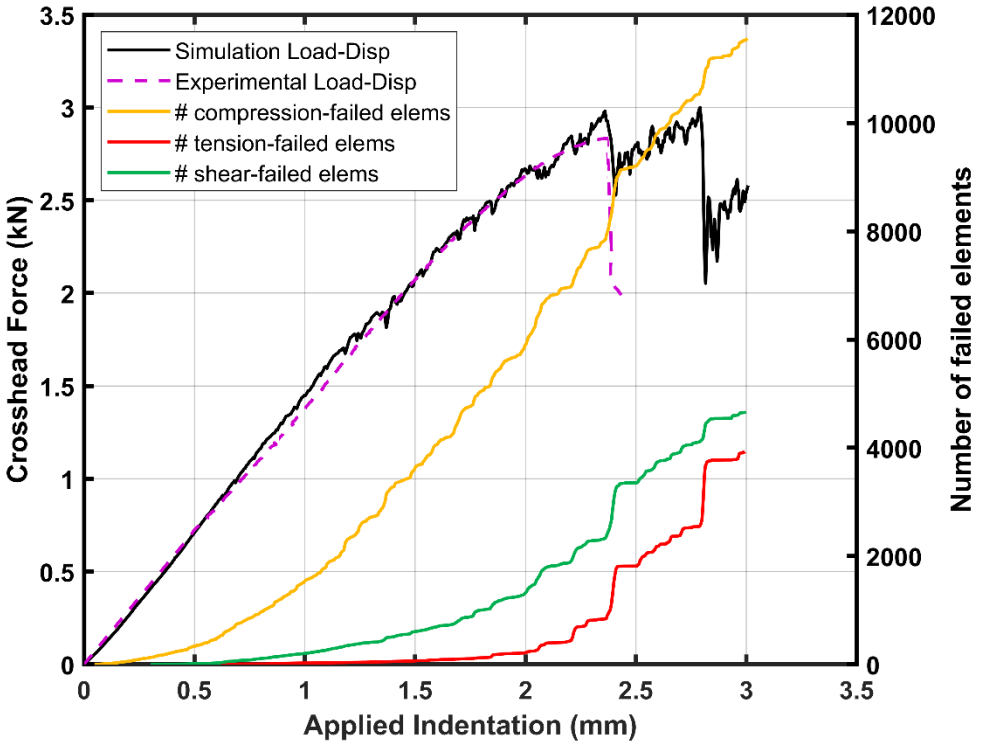

Fig. 9 Load-displacement of Simulation 4 (as in Fig. 7) plotted with the number of elements that failed by compression, tension, or shear

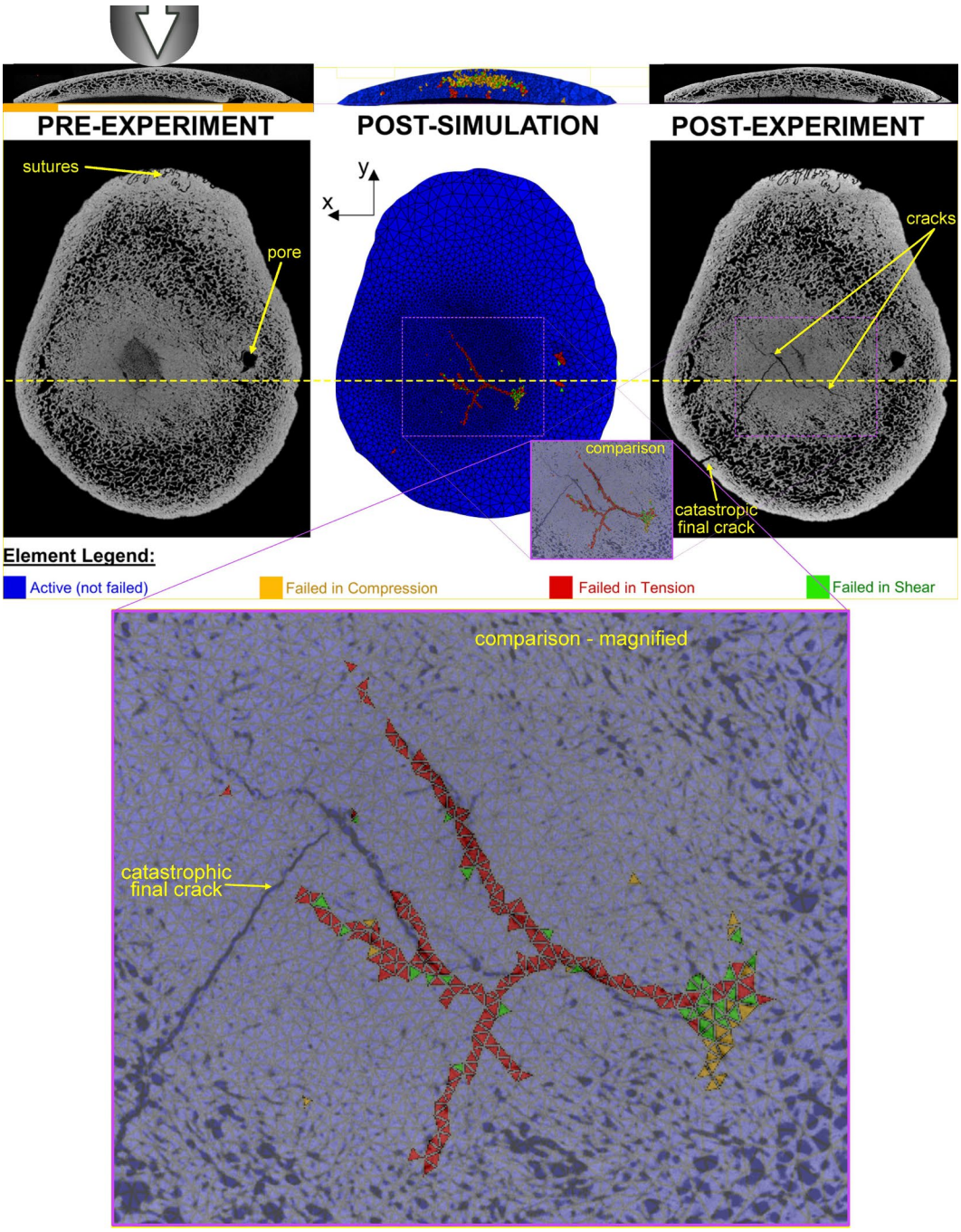

Fig. 10 Comparison of cracking pattern on the specimen backface between experiment and Simulation 4. The experimental cracking pattern is visible in comparing the pre-experiment and post-experiment micro-tomographs (left and right). Dotted line indicates location of cross-sectional images in Fig. 11. Cracking pattern from simulation is visualized by color-coding the elements in the undeformed mesh by their active/failed status at the end of Simulation 4. Element color code matches the colors used in the VUMAT flowchart in Fig. 6 (red = failed in tension, gold = failed in compression, and green = failed in shear). Inset shows overlapping predicted and post-crack patterns, which are remarkably similar on the backface.

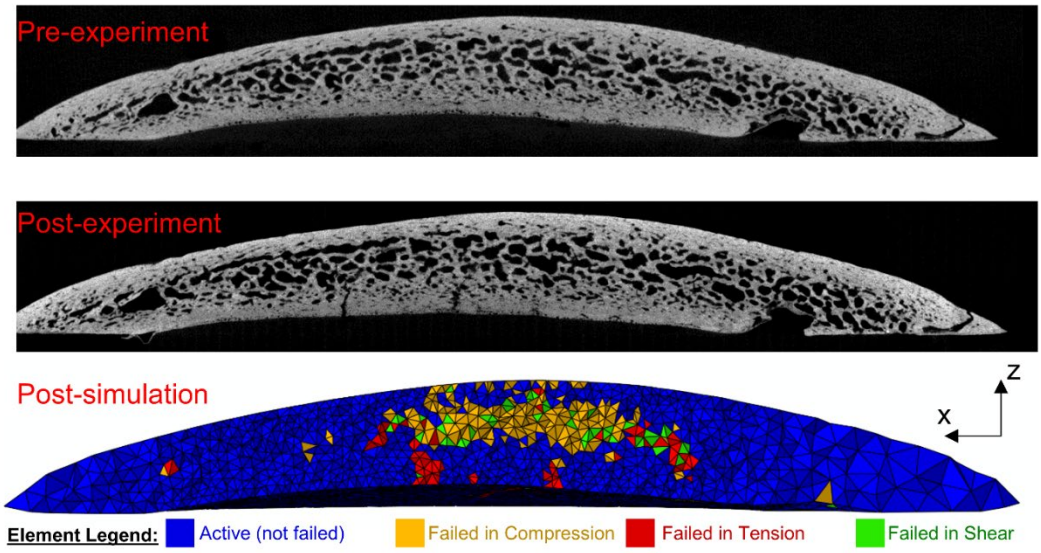

Fig. 11 Comparison of cracking pattern on a cross section (x-z) of the specimen. Location of cross-sectional cut was shown as red dashed line in Fig. 10. Elements in the simulation are color-coded to show active/failed status as in Fig. 10.

4. Discussion

The leading coefficients of Eqs. 1 and 2, E_0 and $\sigma_{f,0}$, correspond to the mechanical properties when BVF = 0, or bone tissue properties. These parameters were iteratively identified in order to match with the experimental load-displacement response of the skullcap indentation, and then further validated with the ability to represent the observed cracking patterns at the end of the experiment. These parameters are summarized in Table 1. In this section, the Young's modulus and strength parameters are first compared with previously published values (Section 4.1). Next, possible reasons for disparities are presented (Section 4.2) before discussing the limitations and assumptions of the current simulation (Section 4.3).

Table 1 BVF-property relationship values for human skull

Property	BVF relationship	Units
Young's modulus	$E = 3 \cdot (f_{BV,0})^{1.6}$	GPa
Density	$\rho_0 = 1.8 \cdot (f_{BV,0})$	g/cm^3
Compressive failure	$\sigma_f^c = 175 \cdot (f_{BV,0})^{2.0}$	MPa
Tensile failure	$\sigma_f^t = 269.4 \cdot (f_{BV,0})^{2.0}$	MPa
Shear failure	$\sigma_f^s = 150 \cdot (f_{BV,0})^{2.0}$	MPa

4.1 Comparing Values for the Young's Modulus and Strength of the Human Skull

Figures 12 and 13 compare the power relationships for Young's modulus (Fig. 12) and failure stresses (Fig. 13) iteratively obtained in the present simulation of skull compression with previously published relationships related to the human skull. The previous relationships were obtained either through direct uniaxial (Boruah et al. 2017; Alexander et al. 2020a) or simple shear (Brown et al. 2020) loading experimentation on human skull specimens. In their experiments, Alexander et al. loaded through-thickness coupons (cores containing the entire thickness of the skull from the inner to outer tables) in quasi-static uniaxial compression. Brown et al. separately deformed coupons of outer table, inner table, and diploë with shear punch tests at low strain-rates. Boruah et al. loaded coupons extracted only from the outer table in uniaxial tension. Conversely, the other two relationships shown in Fig. 12 were derived from loading experiments on bones other than the skull: Zannoni et al. (1999) deformed human femur, while Carter and Hays (1977) loaded both tibia and femur from human and bovine. These relationships are included in Fig. 12 because they have been used by other researchers (Motherway 2012; Chamrad et al. 2018; Haen et al. 2018) to assign element-specific, BVF-dependent moduli to FE models of the human skull.

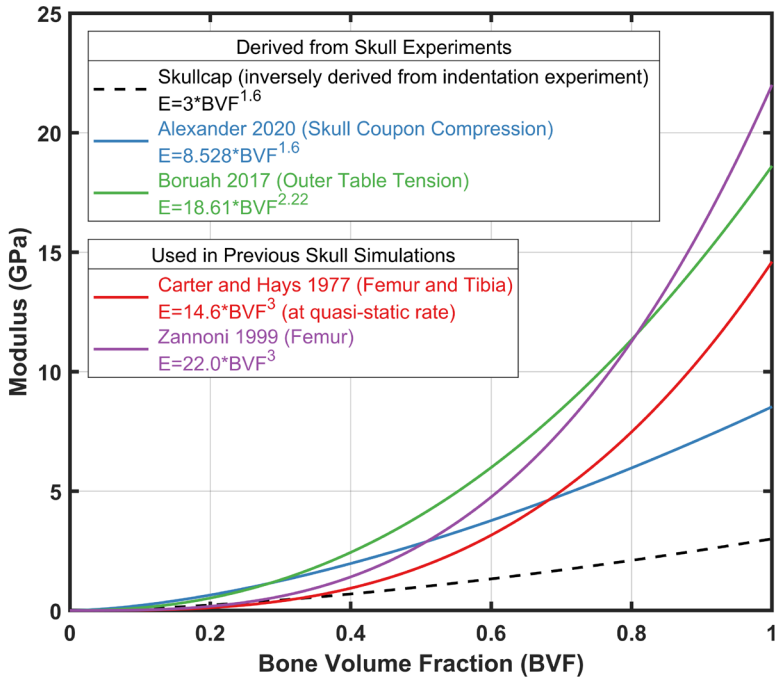

Fig. 12 Modulus power relationships for the human skull, comparing the relationship optimized from the human skullcap simulation (dashed line) with previous relationships (solid lines). Two of the previous relationships were derived from experiments on other bones apart from the skull (Carter and Hays 1977; Zannoni 1999). These are included since they were subsequently used in FE simulations of the skull (Motherway 2012; Chamrad et al. 2018; Haen et al. 2018).

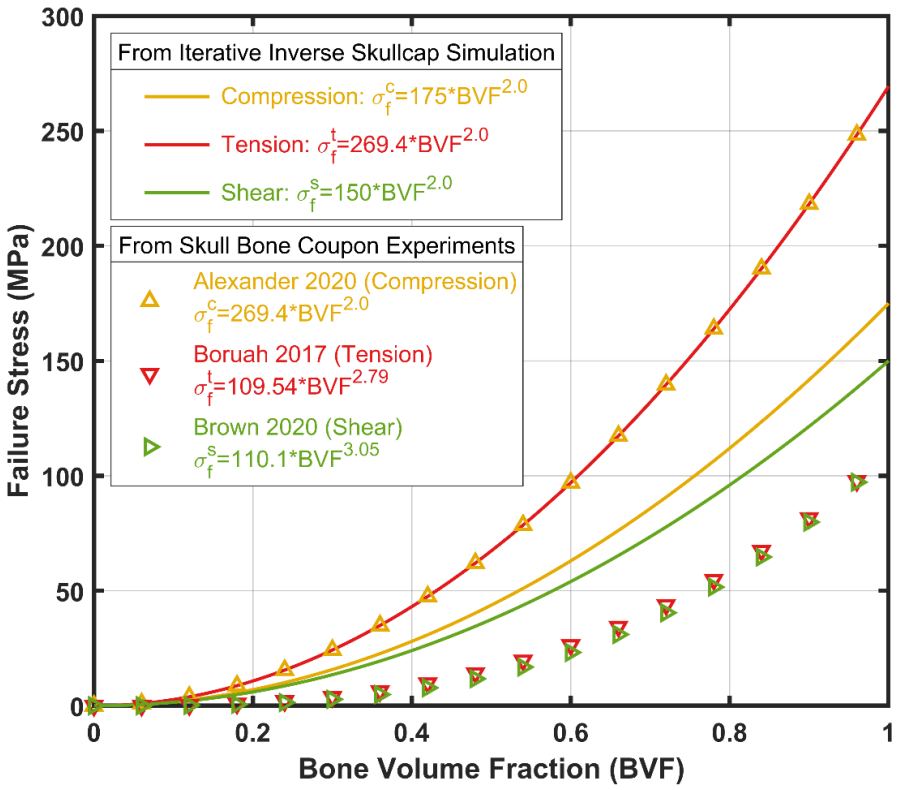

Fig. 13 Power relationships for failure strength of human skull bone. The parameters inversely derived in the present study (solid lines without markers) are compared with previously published experimental relationships on human skull bone (triangular markers). Note the relationship from Brown et al. (2020) shown here was for the shear ultimate stress.

Many previous FE simulations of the human skull modeled the skull sandwich structure by assigning one set of material properties to the cranial cortical bone (outer and inner tables) and a different set to the cranial trabecular bone (diploë). For comparison with those studies and for use in future three-layered simulations, the apparent (averaged) values for the cranial cortical and trabecular bone were calculated by substituting the average BVF of the cortical bone and trabecular bone into the power relationships of Table 1. The average BVF of parietal bone was used since the skullcap specimen used in the experiment of Gunnarsson et al. (2019), which was simulated in this study, was extracted from parietal bone. The average porosities of the outer table, diploë, and inner table in parietal bone are 16%, 63%, and 10%, respectively (Alexander et al. 2019). Therefore, the average BVF of the cortical and trabecular cranial bones is 87% and 37%, respectively. These BVF averages were used to calculate the average mechanical properties for the cortical and trabecular parietal skull bones, as reported in Tables 2 and 3, respectively. Tables 2 and 3 also list previously published values of averaged cortical and trabecular strengths for human skull bone. These values were either measured

through experiments directly on human skull, or were used in FE simulations of the human head and were derived from prior experimentation.

Figures 12 and 13 and Tables 2 and 3 indicate that the mechanical parameters iteratively derived here (inverse of directly deriving from experiments) generally fall within the variation of published values for the human skull, with the exception of the modulus and the tensile strength of the cortical bone. In the present skullcap simulation, the tensile strength was increased to a number higher than the compressive strength to avoid premature catastrophic failure of the specimen. The necessity and effect of this increase in tensile strength was demonstrated in Fig. 7. In Fig. 7, Simulation 2 used a low value of tensile failure strength, which was equal to the compressive strength, but the skullcap catastrophically failed at a premature indentation of about 1.75 mm. Therefore, Simulation 3 used a higher value of tensile failure strength, which postponed macroscopic skullcap failure. At the end of the parameter optimization, the hierarchy of failure strengths indicated that the skullcap was strongest in tension and weakest in shear. Previous studies, as reviewed by Gibson and Ashby (1997) and Morgan et al. (2018), have also shown bone to be weakest in shear, but have reported bone to be stronger in compression than in tension. This difference in tensile strength, together with the difference in moduli values, is further discussed in the following.

Table 2 Failure strengths (megapascals) for the cortical bone of the human skull (outer and inner tables)

Author	Study type	Compression	Tension	Shear
Alexander, current report	Iterative inverse simulation of skullcap indentation	132[a]	204[a]	114[a]
Alexander et al. 2020a	Quasi-static compression of table coupons	220 ± 49	…	…
Boruah et al. 2017	Dynamic tension of outer table coupons	…	65 ± 21	…
Brown et al. 2020	Shear-punch test of outer and inner table (OT, IT) coupons at low rates (10^{-3}–$10^{-1}s^{-1}$)	…	…	OT: 88 ± 9 IT: 73 ± 11
Evans and Lissner 1957	Experiments on embalmed parietal bone coupons	152 ± 109[b]	71	…
McElhaney et al. 1970	Through-thickness coupon experiments	97 ± 36[c]	79 ± 26	…
Raul et al. 2006	Head simulation using experimentally derived strength values	145	90	…
Robbins and Wood 1969	Coupon-level experiments	…	66	…
Sahoo et al. 2013	Head simulation using experimentally derived strength values	132	90	…
Wood 1971	Tension of table coupons at variable strain rates	…	48[d]	…

[a] Calculated for the parietal bone, assuming an average cortical BVF of 87%.
[b] For compression in the longitudinal direction.
[c] Reported as ultimate strength of through-thickness coupon when loaded transverse to the through-thickness axis. Here, the compressive strength of the transversely loaded coupon is assumed to be dominated by the tables.
[d] Calculated for a strain rate of 0.005\s.

Table 3. Failure strengths (megapascals) for the trabecular bone of the human skull (diploë)

Author	Study type	Compression	Tension	Shear
Alexander, current report	Iterative inverse simulation of skullcap indentation	24[a]	37[a]	21[a]
Alexander et al. 2020a	Quasi-static compression of table coupons	32 ± 23[b]	…	…
Brown et al. 2020	Shear-punch test of diploë coupons at low rates (10^{-3}–$10^{-1}s^{-1}$)	…	…	20 ± 3
Evans and Lissner 1957	Experiments on embalmed parietal bone coupons	25	…	…
McElhaney et al. 1970	Through-thickness coupon experiments	74 ± 35[b]	…	21±3
Melvin et al. 1971	Experimentation	32	…	…
Robbins and Wood 1969	Coupon-level experiments	37	…	13[c]
Sahoo et al. 2013	Head simulation using experimentally derived strength values	24.8	34.8	…

[a] Calculated for the parietal bone, assuming an average trabecular BVF of 37%.
[b] Reported as failure stress (Alexander) or ultimate stress (McElhaney) of through-thickness coupons when compressed in the through-thickness direction.
[c] Based on embalmed specimens.

4.2 Inter-Study Comparisons Hindered by Different Experimental Techniques and the Inapplicability of Coupon-Derived Values to Describe Multi-Axial Loading Scenarios

Part of the differences in moduli and strength values just described may be due to different experimental methods and bone materials (anisotropy, chemistry) used by each investigator. For example, the modulus–BVF relationships from Carter and Hays (1977) and Zannoni et al. (1999) were derived from lower-body bones, but modulus–BVF relationships are known to vary by anatomical site (Morgan et al. 2003). In addition, both the compressive modulus and failure stress of bone is known to be strain-rate sensitive (Carter and Hays 1977; Weerasooriya et al. 2016). The skullcap experiment simulated in the present study was at a quasi-static rate, whereas the modulus–BVF and strength–BVF curves of Boruah et al. (2017) were derived from dynamic tests conducted at rates above 100/s. Furthermore, some of the studies cited in Tables 2 and 3 used only embalmed bone, but embalming the bone may alter its mechanical properties, especially in compression (McElhaney et al. 1964; Öhman et al. 2008).

However, the current values inversely derived from the skullcap simulation also differed even when compared with experiments on fresh bone at quasi-static loading rates using modern instrumentation and techniques. For example, the first iterations of the skullcap simulation (e.g., Simulation 1, Fig. 7) used the modulus–BVF relationship from Alexander et al. (2020a) derived from quasi-static compression of fresh coupons. However, this starting relationship yielded a response, which was too stiff, and the leading coefficient was eventually reduced from 8.528 to 3.0 GPa (Simulation 2, Fig. 7). This difference may be due to the many assumptions employed in deriving the modulus–BVF relationship from the experiments. It also emphasizes the difference in using values derived from simple coupon-level uniaxial experiments to describe the response (deformation and failure) of the material in the different, multi-axial loading environment of the skullcap indentation experiments. The inability to validate the deformation and then failure of critically designed multi-axial loading experiments, using material models only obtained from uniaxial experiments at different stress-states, opens the following question: Should we focus on inversely obtaining the material models using a few theory-critical validation experiments rather than deriving them from uniaxial constant strain-rate studies at different simple stress-states such as tension, compression, and shear?

4.3 Limitations and Assumptions

The current study was limited to one specimen from a donor of advanced age. Coronal sutures passed through the anterior of the specimen. The micro-architecture of the sutures was not well-reflected in the BVF distribution of the FE mesh, since the element size was particularly large closer to the periphery of the specimen (Fig. 5), where most of the sutures were located. However, in the indentation experiment, the presence of the sutures did not appear to affect the cracking pattern. The sutures were in the anterior portion of the skullcap, away from the area where the cracks were centralized (Fig. 10).

There were several limiting assumptions involved with the implementation of the FE modeling concept that was used. First, the Poisson's ratio was assumed to be constant and invariant with the BVF of the element. Therefore, elements in the outer and inner tables were assumed to have the same Poisson's ratio as elements in the diploë. However, the apparent Poisson's ratio (ν_{app}) of elements consisting of both bone and pores may be a function of the BVF of the element. Moreover, the ν_{app}-BVF function may have different scaling parameters than the E-BVF relationship as suggested, for example, by the work of Yang et al. (1998) and Yoon et al. (2002). Implementing a ν_{app}-BVF scaling relationship in the skullcap

simulation could cause the diploë to exhibit a softer response under compression. It was noted that one difference between the current study and previous literature was that in the current study, bone was modeled as stronger in tension than in compression. A softer diploë would have enabled a higher compressive strength threshold to be used in the simulation, perhaps even higher than the tensile strength threshold. In addition, since the Poisson's ratio was constant in the present study, the bulk modulus was scaled by the BVF with the same exponential factor as the Young's modulus (see Eq. 14). However, the bulk modulus could conceivably scale differently with the BVF, especially if a ν_{app}-BVF scaling relationship was implemented with different scaling parameters than the E-BVF relationship. The difference between the BVF scaling of the bulk and Young's moduli would influence the post-failure behavior of the elements. Future work could examine these effects of implementing a ν_{app}-BVF scaling relationship.

The indentation in the experiment was applied at a quasi-static rate of 5×10^{-6} m/s but was simulated at a nominal velocity of 0.33 m/s. This velocity was required to reduce the large computational expense arising from the small time increment of the explicit FE method. The use of this finite velocity was not expected to noticeably change the response, since the material models were not rate-dependent. As shown in Appendix B, the kinetic energy accounted for only a small fraction of the total internal energy during the simulation, and did not appear to noticeably affect the load-displacement response.

Other assumptions included those inherent to the VUMAT procedure, which was implemented for modeling failure at an element-by-element basis. These assumptions have been previously discussed. In addition, simulations were prone to abort early due to severe distortion of some elements, which had previously failed and were no longer load-bearing. Converting failed elements to particles via the smoothed-particle hydrodynamics method could enable the simulation to continue beyond initiation of failure and obviate the problem of element distortion with large deformations associated with post-failure and propagation of fracture. Finally, the simulation is likely dependent on the mesh and on the position of the indenter/impactor. In the experiment, the POI was nominally located at the skullcap apex (Fig. 5C), but the exact experimental POI could not be precisely identified and modeled in the simulation. Appendix C demonstrates the effect of small deviations in the POI location, with the corresponding element failure. The overall cracking shows the same directional trend, and the effect of small deviations in POI location on the initial linear portion of the simulation is negligible.

The parameter values obtained for the modulus and strength power relationships were dependent on the FE approximations outlined previously and on the assumed functional forms of the relationships. Moreover, there is no guarantee as to the uniqueness of values obtained here for the leading coefficients and exponents in the power relationships, since different combinations of these parameters could lead to similar simulation outcomes.

5. Conclusion and Future Work

The nonlinear load-displacement response of the human skull was simulated by modeling material heterogeneity on an element-by-element basis (elemental scale) using a microstructurally inspired material deformation model. In addition, each element was allowed to fail by any of the three possible mechanisms: tensile, compressive, or shear, corresponding to linear, depressed, or shear-penetration macro-cracks, respectively, and which were activated by different stress-states. Failure under each dominant stress-state was represented with a microstructurally inspired failure model. During indentation, elements were allowed to fail when the max tension, max compression, or max shear exceeded their threshold stresses corresponding to the linear, depressed, or shear penetration-failure mechanisms, respectively. Threshold stresses were derived from different failure models based on the microstructural details of the element. These failure stresses, together with microstructure-dependent moduli, were assigned to each element through power relationships.

The parameters of the power relationships were obtained through iterative simulations, rather than directly from experiments as is the usual procedure, to match the derived load-displacement with that which was experimentally measured. The final set of model parameters is shown in Table 1. The starting values of these parameters for the first iterations were taken from previous experimental and numerical studies of bone coupons. However, these coupon-level moduli and failure stresses had to be iterated before the skullcap simulation was able to match the multi-axial indentation experimental response. The inability of the values derived from coupon-level studies to model the skullcap response a priori could indicate the inapplicability of parameters derived at the coupon-level to predict the response of bone in a multi-axial loading state, which more closely represents the in vivo loading environment.

Having developed and demonstrated the simulation methodology at the skullcap-specimen level, the next step is implementing material heterogeneity within a larger-scale mesh of the entire skull. As was done within the skullcap, an impact zone can be identified at the point of contact with the skull. The element-specific

modeling procedure can be applied within this zone, with a more homogeneous approach taken elsewhere to limit computational expense. Automated software can be used to facilitate the mapping of the FE mesh to the tomography and the assignment of microstructure-dependent properties, as demonstrated here with the MIS.

The ability to model the nonlinear response and initiation of fracture of human skull can be used to carry out in silico parametric studies, varying impactor type (e.g., cone angle) and velocity. The tool described here can be used to predict skull fracture initiation, which can serve as a readily identifiable injury criteria, and the risk of head injury can be predicted for various loading configurations.

Future work will include extending the validated concepts and models for higher loading rates, and then to use these rate-dependent, MIMB models to obtain failure initiation mechanisms maps as a function of indenter velocity and its geometry.

6. References

Alexander SL, Gunnarsson CA, Rafaels K, Weerasooriya T. Multiscale response of the human skull to quasi-static compression. Journal of the Mechanical Behavior of Biomedical Materials. 2020a;102.

Alexander SL, Weerasooriya T. Micro-CT-based three-layer finite element model for quasi-static human skull impact. DEVCOM Army Research Laboratory (US); 2020 May. Report No.: ARL-TR-8962.

Alexander SL, Rafaels K, Gunnarsson CA, Weerasooriya T. Structural analysis of the frontal and parietal bones of the human skull. Journal of the Mechanical Behavior of Biomedical Materials. 2019;90:689–701.

Alexander SL, Weerasooriya T. Microstructure-based model of the deformation and failure response of the human skull under uniaxial compression. DEVCOM Army Research Laboratory; 2020a. Report No.: ARL-TR-8961. Also under review by the Journal of the Mechanical Behavior of Biomedical Materials.

Auperrin A, Delille R, Lesueur D, Bruyère K, Masson C, Drazétic P. Geometrical and material parameters to assess the macroscopic mechanical behaviour of fresh cranial bone samples. Journal of Biomechanics. 2014;47(5):1180–1185.

Bessho M, Ohnishi I, Matsuyama J, Matsumoto T, Imai K, Nakamura K. Prediction of strength and strain of the proximal femur by a CT-based finite element method. Journal of Biomechanics. 2007;40(8):1745–1753.

Boruah S, Henderson K, Subit D, Salzar R, Shender B, Paskoff G. Response of human skull bone to dynamic compressive loading. In: Proceedings of the International Research Council on Biomechanics of Injury (IRCOBI) Conference; 2013 Sep; Gothenburg, Sweden. Vol. 13. p. 497.

Boruah S, Subit DL, Paskoff GR, Shender BS, Crandall JR, Salzar RS. Influence of bone microstructure on the mechanical properties of skull cortical bone—a combined experimental and computational approach. Journal of the Mechanical Behavior of Biomedical Materials. 2017;65:688–704.

Brown A, Rafaels KA, Weerasooriya T. Microstructural and rate-dependent shear response of human skull bones. DEVCOM Army Research Laboratory; 2020 Mar. Report No.: ARL-TR-8925. Also in review at the Journal of the Mechanical Behavior of Biomedical Materials.

Carter DR, Hayes WC. The compressive behavior of bone as a two-phase porous structure. The Journal of Bone and Joint Surgery. 1977;59(7):954–962.

Chamrad J, Marcián P, Borák L. On the level of computational model of a human skull: a comparative study. Applied and Computational Mechanics. 2018;12(1):5–16.

Cotton RT, Pearce CW, Young PG, Kota N, Leung AC, Bagchi A, Qidwai SM. Development of a geometrically accurate and adaptable finite element head model for impact simulation: the Naval Research Laboratory–Simpleware Head Model. Computer Methods in Biomechanics and Biomedical Engineering. 2016;19(1):101–113.

Deck C, Willinger R. Improved head injury criteria based on head FE model. International Journal of Crashworthiness. 2008;13(6):667–678.

DiMaio VJM. Gunshot wounds: practical aspects of firearms, ballistics and forensic techniques. 2nd ed. CRC Press; 1999.

Enns-Bray WS, Bahaloo H, Fleps I, Ariza O, Gilchrist S, Widmer R, Guy P, Pálsson H, Ferguson SJ, Cripton PA, Helgason B. Material mapping strategy to improve the predicted response of the proximal femur to a sideways fall impact. Journal of the Mechanical Behavior of Biomedical Materials. 2018;78:196–205.

Evans FG, Lissner HR. Tensile and compressive strength of human parietal bone. Journal of Applied Physiology. 1957;10(3):493–497.

Gibson LJ, Ashby MF. Cellular solids: structure and properties. Cambridge University Press; 1997.

Gunnarsson CA, Alexander S, Rafaels K, Walter T, Weerasooriya T. High-rate fracture of human skull. Mechanics of Biological Systems & Micro-and Nanomechanics. 2019;4:91–94.

Hambli R. Micro-CT finite element model and experimental validation of trabecular bone damage and fracture. Bone. 2013;56(2):363–374.

Haen P, Dubois G, Goudot P, Schouman T. Comparative finite element analysis of skull mechanical properties following parietal bone graft harvesting in adults. Journal of Cranio-Maxillofacial Surgery. 2018;46(2):329–337.

Helgason B, Gilchrist S, Ariza O, Chak JD, Zheng G, Widmer RP, Ferguson SJ, Guy P, Cripton PA. Development of a balanced experimental–computational approach to understanding the mechanics of proximal femur fractures. Medical Engineering & Physics. 2014;36(6):793–799.

Hubbard RP. Flexure of layered cranial bone. Journal of Biomechanics. 1971;4(4):251–263.

Knowles NK, Langohr GD, Faieghi M, Nelson A, Ferreira LM. Development of a validated glenoid trabecular density-modulus relationship. Journal of the Mechanical Behavior of Biomedical Materials. 2019;90:140–145.

Lozano-Mínguez E, Palomar M, Infante-García D, Rupérez MJ, Giner E. Assessment of mechanical properties of human head tissues for trauma modelling. International Journal for Numerical Methods in Biomedical Engineering. 2018;34(5):e2962.

McElhaney J, Fogle J, Byars E, Weaver G. Effect of embalming on the mechanical properties of beef bone. Journal of Applied Physiology. 1964;19(6):1234–1236.

McElhaney JH, Fogle JL, Melvin JW, Haynes RR, Roberts VL, Alem NM. Mechanical properties of cranial bone. Journal of Biomechanics. 1970;3(5):495–511.

Melvin JW, Robbins DH, Roberts VL. The mechanical behavior of the diploë layer of the human skull in compression. Dev Mech. 1969;5:811–818. Cited in: Wood JL. Dynamic response of human cranial bone. Journal of Biomechanics. 1971;4.1:1–12.

Morgan EF, Bayraktar HH, Keaveny TM. Trabecular bone modulus density relationships depend on anatomic site. J Biomech. 2003;36(7):897–904.

Morgan EF, Unnikrisnan GU, Hussein AI. Bone mechanical properties in healthy and diseased states. Annual Review of Biomedical Engineering. 2018;20:119–143.

Motherway JA. The dynamic mechanical behaviour of cranial bone [Doctoral thesis]. University College Dublin; 2012.

Motherway JA, Verschueren P, Van der Perre G, Vander Sloten J, Gilchrist MD. The mechanical properties of cranial bone: the effect of loading rate and cranial sampling position. Journal of Biomechanics. 2009;42(13):2129–2135.

Mow VC, Huiskes R. Basic orthopaedic biomechanics and mechano-biology. 3rd ed. Baltimore (MD): Lippincott Williams and Wilkins; 2005.

Öhman C, Dall'Ara E, Baleani M, Jan SV, Viceconti M. The effects of embalming using a 4% formalin solution on the compressive mechanical properties of human cortical bone. Clinical Biomechanics. 2008;23(10):1294–1298.

Ptak M, Ratajczak M, Kwiatkowski A, Sawicki M, Wilhelm J, Fernandes FA, Druszcz A. Investigation of biomechanics of skull structures damages caused by dynamic loads. Acta of Bioengineering and Biomechanics. 2018;20(4):143–150.

Raul JS, Baumgartner D, Willinger R, Ludes B. Finite element modelling of human head injuries caused by a fall. International Journal of Legal Medicine. 2006;120(4):212–218.

Robbins DH, Wood JL. Determination of mechanical properties of the bones of the skull. Experimental Mechanics. 1969;9(5):236–240.

Robson Brown K, Tarsuslugil S, Wijayathunga VN, Wilcox RK. Comparative finite-element analysis: a single computational modelling method can estimate the mechanical properties of porcine and human vertebrae. Journal of the Royal Society Interface. 2014;11(95):20140186.

Sahoo D, Deck C, Yoganandan N, Willinger R. Anisotropic composite human skull model and skull fracture validation against temporo-parietal skull fracture. Journal of the Mechanical Behavior of Biomedical Materials. 2013;28:340–353.

Sanborn B, Gunnarsson CA, Foster M, Weerasooriya T. Quantitative visualization of human cortical bone mechanical response: studies on the anisotropic compressive response and fracture behavior as a function of loading rate. Experimental Mechanics. 2016;56(1):81–95.

Shannahan L, Weerasooriya T, Gunnarsson A, Sanborn B, Lamberson L. Rate-dependent fracture modes in human femoral cortical bone. International Journal of Fracture. 2015;194(2):81–92.

Taddei F, Schileo E, Helgason B, Cristofolini L, Viceconti M. The material mapping strategy influences the accuracy of CT-based finite element models of bones: an evaluation against experimental measurements. Medical Engineering & Physics. 2007;29(9):973–979.

Tse KM, Tan LB, Lee SJ, Lim SP, Lee HP. Development and validation of two subject-specific finite element models of human head against three cadaveric experiments. International Journal for Numerical Methods in Biomedical Engineering. 2014;30(3):397–415.

Weerasooriya T, Sanborn B, Gunnarsson CA, Foster M. Orientation dependent compressive response of human femoral cortical bone as a function of strain rate. Journal of Dynamic Behavior of Materials. 2016;2(1):74–90.

Wood JL. Dynamic response of human cranial bone. Journal of Biomechanics. 1971;4(1):1–12.

Yang G, Kabel J, Van Rietbergen B, Odgaard A, Huiskes RI, Cown SC. The anisotropic Hooke's law for cancellous bone and wood. Journal of Elasticity. 1998;53(2):125–46.

Yoon YJ, Yang G, Cowin SC. Estimation of the effective transversely isotropic elastic constants of a material from known values of the material's orthotropic elastic constants. Biomechanics and Modeling in Mechanobiology. 2002;1(1):83–93.

Zannoni C, Mantovani R, Viceconti M. Material properties assignment to finite element models of bone structures: a new method. Medical Engineering & Physics. 1999;20(10):735–740.

Appendix A. Parametric Study of the Modulus and Failure Strength Power Relationships

The modulus and failure strengths were calculated for each element using power relationships which scaled the bone volume fraction (BVF) of the element. The functional forms of these relationships are reproduced here for reference as Eq. A-1 (modulus), Eq. A-2 (compressive failure stress), Eq. A-3 (tensile failure stress), and Eq. A-4 (shear failure stress):

$$E = E_0 \cdot \left(f_{BV,0}\right)^k \tag{A-1}$$

$$\sigma_f^c = \sigma_{f,0}^c \cdot \left(f_{BV,0}\right)^m \tag{A-2}$$

$$\sigma_f^t = \sigma_{f,0}^t \cdot \left(f_{BV,0}\right)^n \tag{A-3}$$

$$\sigma_f^s = \sigma_{f,0}^s \cdot \left(f_{BV,0}\right)^p \tag{A-4}$$

For simplicity, throughout this appendix, the original bone volume fraction ($f_{BV,0}$) will also be written as BVF. Each power relationship had two parameters: a leading coefficient and an exponent factor. These parameters were determined through iterative simulations. Figure A-1 summarizes the effects of these parameters by comparing the load-displacement of four different simulations with the experimentally measured response. Figure A-1 is a copy of Fig. 7, where the methods of calculating load and displacement were presented. As in Fig. 7, the four simulations are referred to throughout this appendix as Simulations 1–4. The power relationships for modulus and failure strengths are presented for these four simulations in Table A-1.

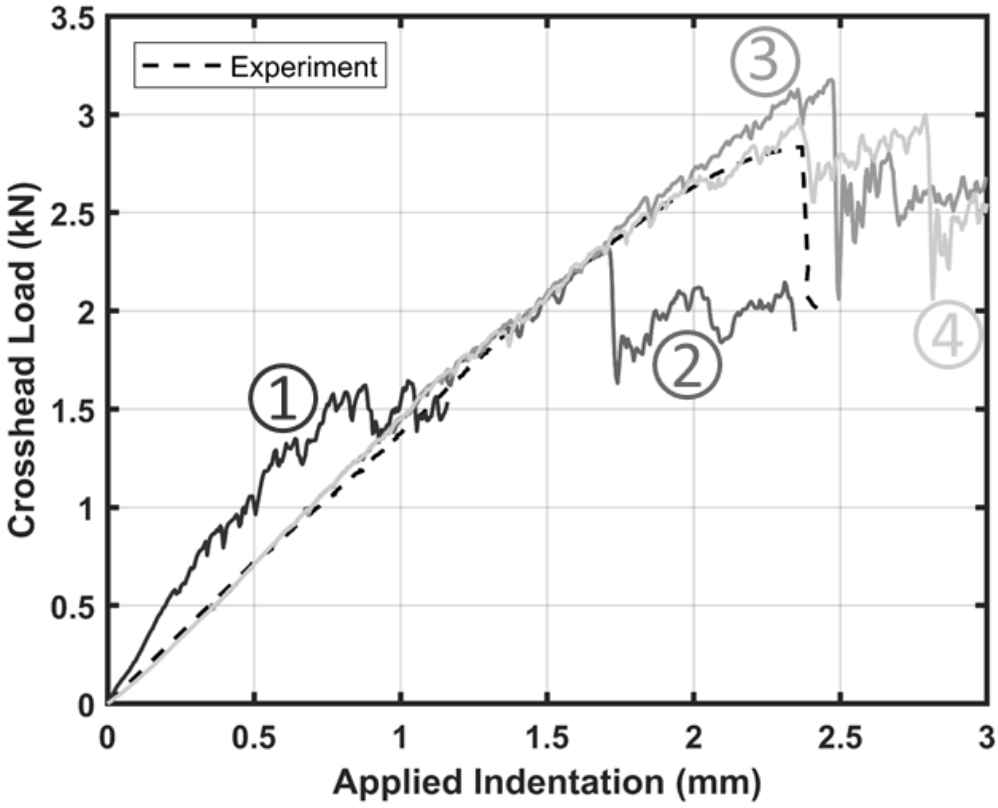

Fig. A-1 Summary of load-displacement effect of changing the power-law relationship parameters (Table A-1).

Table A-1 Power relationships used in Simulations 1–4

Simulation	Modulus (GPa)	Comp. failure (MPa)	Tensile failure (MPa)	Shear failure (MPa)
1	$8.525(f_{BV,0})^{1.6}$	$175(f_{BV,0})^{2.0}$	$175(f_{BV,0})^{2.0}$	…
2	$3.0(f_{BV,0})^{1.6}$	$175(f_{BV,0})^{2.0}$	$175(f_{BV,0})^{2.0}$	…
3	$3.0(f_{BV,0})^{1.6}$	$175(f_{BV,0})^{2.0}$	$269.4(f_{BV,0})^{2.0}$	…
4	$3.0(f_{BV,0})^{1.6}$	$175(f_{BV,0})^{2.0}$	$269.4(f_{BV,0})^{2.0}$	$150(f_{BV,0})^{2.0}$

As a starting point, Simulation 1 used previously published power relationships for modulus and for compressive and tensile failure, and assumed that no elements failed in shear. The modulus relationship was from an experimental study on the

compressive modulus of human skull bone coupons: $E = 8.525*\text{BVF}^{1.6}$ GPa.[1] One of the experiments used to derive the modulus relationship was later simulated by Alexander and Weerasooriya[2] and compressive and tensile failure strengths were iteratively identified as $\sigma_f^c = \sigma_f^t = 175*\text{BVF}^{2.0}$ MPa. This power relationship was likewise used for the compressive and tensile failure strengths in Simulation 1.

As shown in Fig. A-1, the load-displacement response of Simulation 1 was too stiff. Therefore, the leading coefficient of Eq. A-1 (E_0) was decremented while maintaining the exponent factor of $k = 1.6$. The effect of decrementing the modulus is shown in Fig. A-2, where the final value of the leading coefficient was $E_0 = 3$GPa (identical to Simulation 2). The skullcap stiffness in Simulation 2 closely matched the initial stiffness of the experiment.

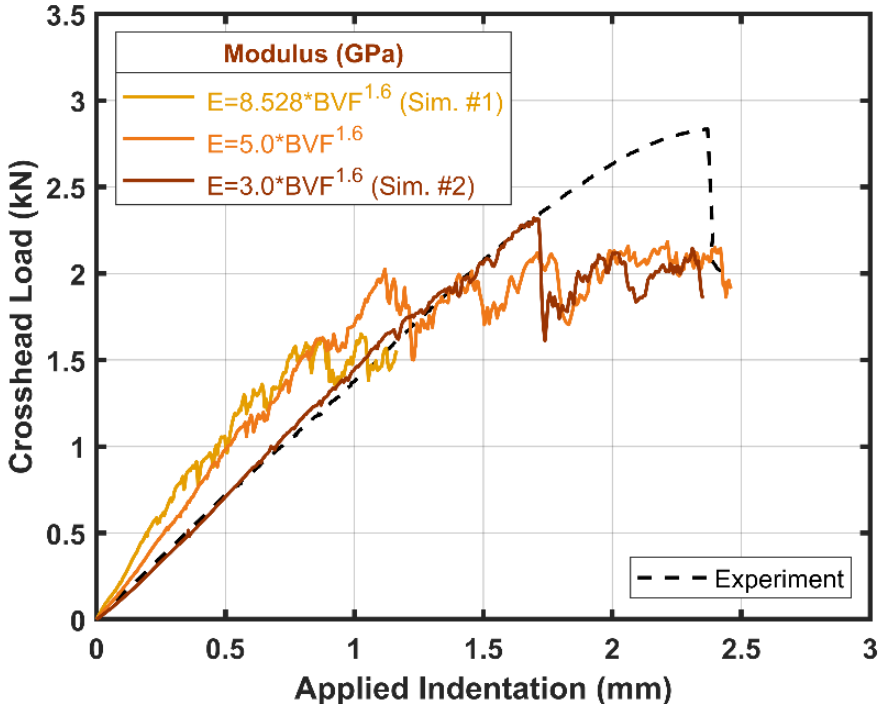

Fig. A-2 Effect of changing the leading coefficient (E_0) of the power law for the modulus. For these three simulations, the compressive and tensile failure power relationships were given by $\sigma_f^c = \sigma_f^t = 175*\text{BVF}^{2.0}$, and there was no shear failure considered.

[1] Alexander SL, Gunnarsson CA, Rafaels K, Weerasooriya T. Multiscale response of the human skull to quasi-static compression. Journal of the Mechanical Behavior of Biomedical Materials. 2020;102.

[2] Alexander SL, Weerasooriya T. Microstructure-based model of the deformation and failure response of the human skull under uniaxial compression. DEVCOM Army Research Laboratory; 2020a. Report No.: ARL-TR-8961. Also under review by the Journal of the Mechanical Behavior of Biomedical Materials.

However, Simulation 2 failed prematurely, with load sharply decreasing at an indentation of approximately u_y = 1.71 mm. This decrease corresponded to the specimen rupturing (macroscopic failure): a crack traversed the entire thickness of the specimen from the inner to the outer table. This rupture was premature compared with the experiment, which ruptured at approximately u_y = 2.37 mm (the rupture in the experiment was described in Section 3). Figure A-3 shows the number of elements failed by the three different modes during the simulation, and indicates that the premature rupture of Simulation 2 corresponded to a large number of elements failing in tension. Therefore, the leading coefficient of tensile failure strength ($\sigma_{f,0}^t$, Eq. A-3) was next increased from $\sigma_{f,0}^t$ = 175 MPa (as in Simulations 1 and 2) to the value of $\sigma_{f,0}^t$ = 269.4 MPa (Simulation 3). The effect of this increase in $\sigma_{f,0}^t$ is shown in Fig. A-4. The higher value of $\sigma_{f,0}^t$ = 269.4 MPa was chosen based on the experimental study of human skull bone coupons.[1] There, the failure stress of human skull bone specimens loaded in compression was plotted as a function of the BVF of the specimens. A power-law was optimized to relate the failure stress to the BVF, while constraining the exponent factor to a value of 2. The leading coefficient was calculated to be 269.4 MPa.

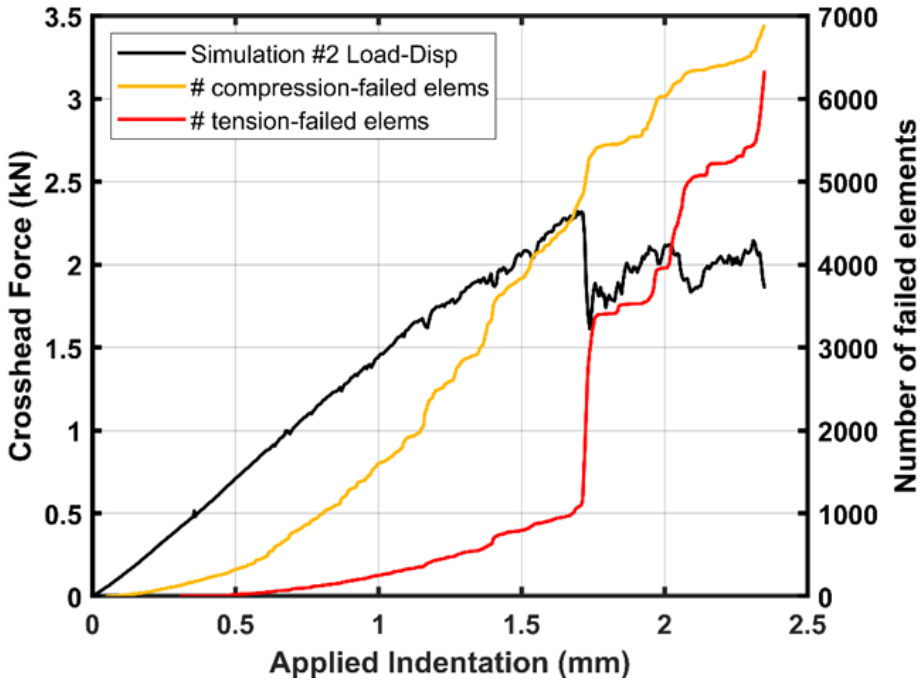

Fig. A-3 Number of elements failed in compression and tension as a function of applied indentation for Simulation 2. Skullcap rupture at an applied indentation of 1.71 mm corresponded with a sharp increase in the number of elements that failed in tension. Therefore, Simulation 3 used a higher value for leading coefficient of the tensile-failure power relationship.

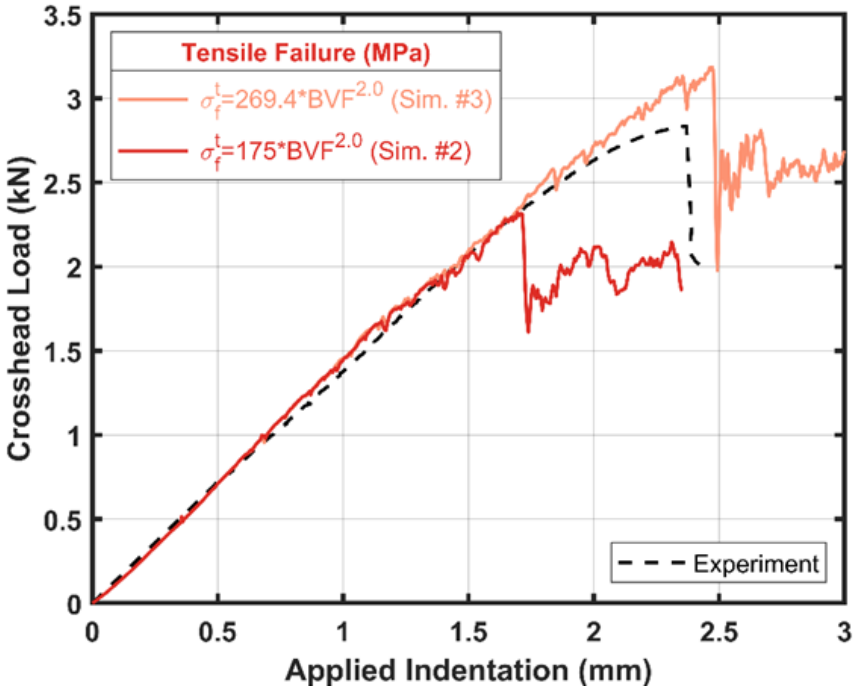

Fig. A-4 Effect of changing the leading coefficient of the power law for tensile failure. For both of these simulations, the modulus power relationship was E = 3.0*BVF$^{2.0}$ GPa; the compressive power relationship was σ_f^c = 175*BVF$^{2.0}$ MPa, and no shear failure was considered.

Finally, Fig. A-5 shows the effect of varying the shear-failure leading coefficient ($\sigma_{f,0}^s$) and exponent factor, p (Eq. A-4). The initial power relationship for shear failure was taken from experiments of Brown et al.[3] using shear punch test on human skull specimens. A preliminary relationship from those experiments related the shear ultimate stress, τ, to the BVF of the specimens by: τ = 115.9*BVF$^{3.797}$. Based on this relationship, early simulation iterations including shear failure used an exponent factor of p = 3.797 (purple curves in Fig. A-5). However, in these simulations, the skullcap ruptured prematurely due to a high number of elements failing in shear. To avoid premature failure, the leading coefficient had to be increased to a very high number ($\sigma_{f,0}^s$ ~ 400 MPa). For simplicity, trial simulations were run with the exponent factor, p, set to match the exponent factor used for both compression and shear: p = m = n = 2.0 (green curves of Fig. A-5). A favorable load-displacement curve and cracking pattern was identified using the relationship of σ_f^s = 150*BVF$^{2.0}$, which was used in Simulation 4.

[3] Brown A, Rafaels KA, Weerasooriya T. Microstructural and rate-dependent shear response of human skull bones. DEVCOM Army Research Laboratory; 2020 Mar. Report No.: ARL-TR-8925. Also in review at the Journal of the Mechanical Behavior of Biomedical Materials.

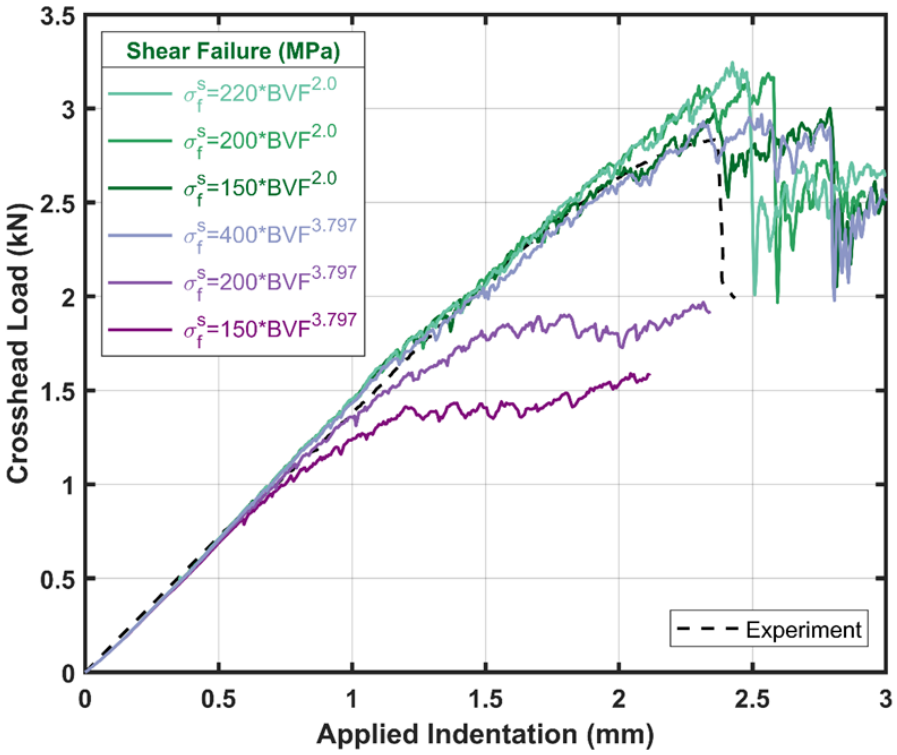

Fig. A-5 Effect of changing the leading coefficient of the power law for shear failure. For all of these simulations, the modulus power relationship was E = 3.0*BVF$^{2.0}$ GPa, the compressive failure power relationship was σ_f^c = 175*BVF$^{2.0}$ MPa, and the tensile failure power relationship was σ_f^t = 269.4*BVF$^{2.0}$ MPa.

Note that using a leading coefficient of $\sigma_{f,0}^s$ = 220 MPa (light green curve in Fig. A-4 with highest peak load) caused only five elements to fail in shear. Another simulation was run with $\sigma_{f,0}^s$ = 230 MPa, for which no elements failed in shear, and the load-displacement curve exactly matched the result of Simulation 3 (no shear failure).

Appendix B. Effect of the Finite (Non-Quasi-Static) Velocity of Indenter/Impactor

The indentation experiment was conducted at a quasi-static rate, but in the simulation the indenter/impactor was displaced at a nominal velocity of 0.33 m/s. As a means of quantifying the effect of this nonzero velocity, the kinetic energy (KE) and internal energy (IE) of the finite-element (FE) model were extracted from Simulation 4. The ratio of KE/IE can indicate the applicability of the FE simulation in modeling the quasi-static experiment.[1] Figure B-1 demonstrates the effect of the KE/IE ratio on the load displacement in the simulation. After an initial spike when the indenter/impactor contacts the specimen, the ratio remains well below 5%.

[1] Gulavani O, Hughes K, Vignjevic R. Explicit dynamic formulation to demonstrate compliance against quasi-static aircraft seat certification loads (CS25. 561). Part I: influence of time and mass scaling. Proceedings of the Institution of Mechanical Engineers, Part G: Journal of Aerospace Engineering. 2014;228(11):1982–1995.

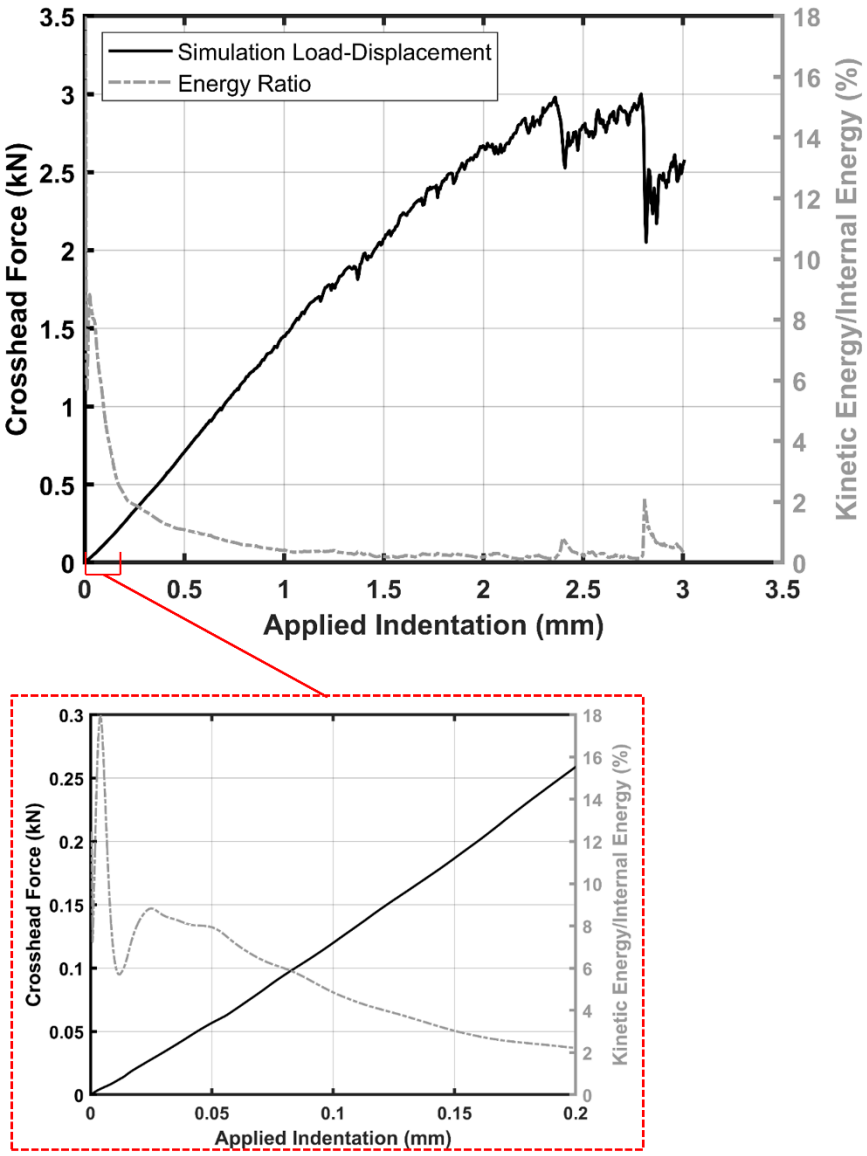

Fig. B-1 Ratio of KE to total energy during the simulation of skullcap indentation, together with the simulation load displacement

Appendix C. Effect of Changing the Indenter/Impactor Point of Contact with the Skullcap (POI)

The point of contact between the indenter/impactor and the skullcap (point of indentation/impact, POI), was nominally at the apex of the skullcap, which was the location in the transverse x-y plane where the specimen rose the highest in the z-direction (Fig. 5 in the main report). However, there was uncertainty in identifying the exact location of the experimental POI and modeling this location in the simulation. Therefore, the effect in the simulation of changing the POI location was examined by re-simulating Simulation 4 using a POI displaced by 7.63 mm in the transverse x-y plane (Fig. C-1).

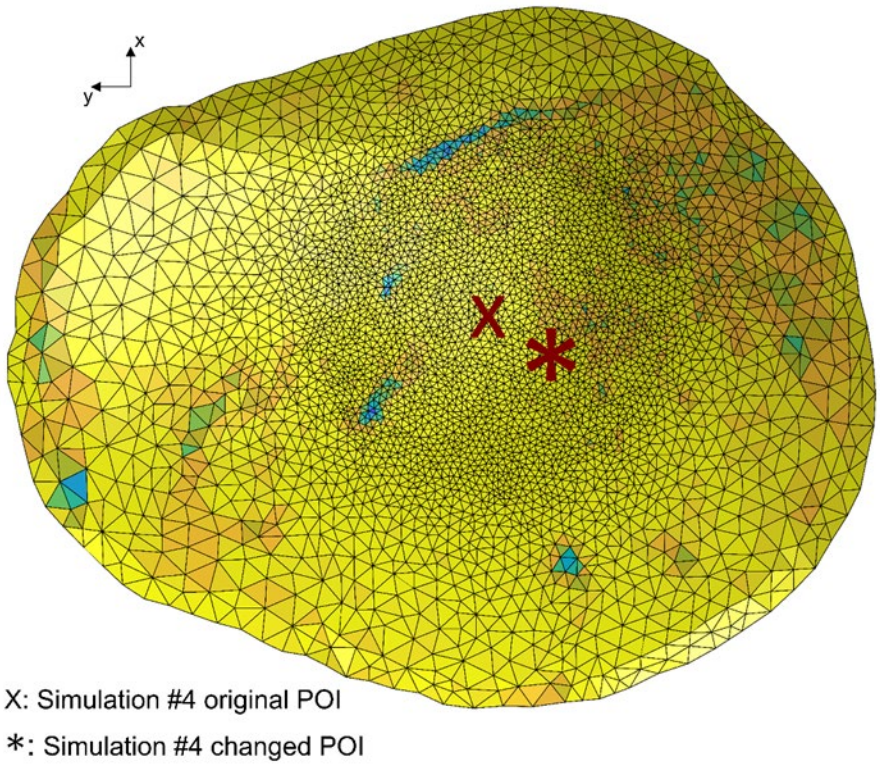

Fig. C-1 Top-down view of the skullcap mesh with the original and changed POI locations marked. Distance in the x-y plane between the two POI locations was 7.63 mm.

Figure C-2 shows the effect on the load-displacement response of changing the POI. As a result of changing the POI, the simulation aborted prematurely at an applied displacement of u_y = 2.23 mm due to element distortion. Figure C-3 compares the backface cracking pattern for the simulations with the two different POI locations at the applied displacement of u_y = 2.23 mm.

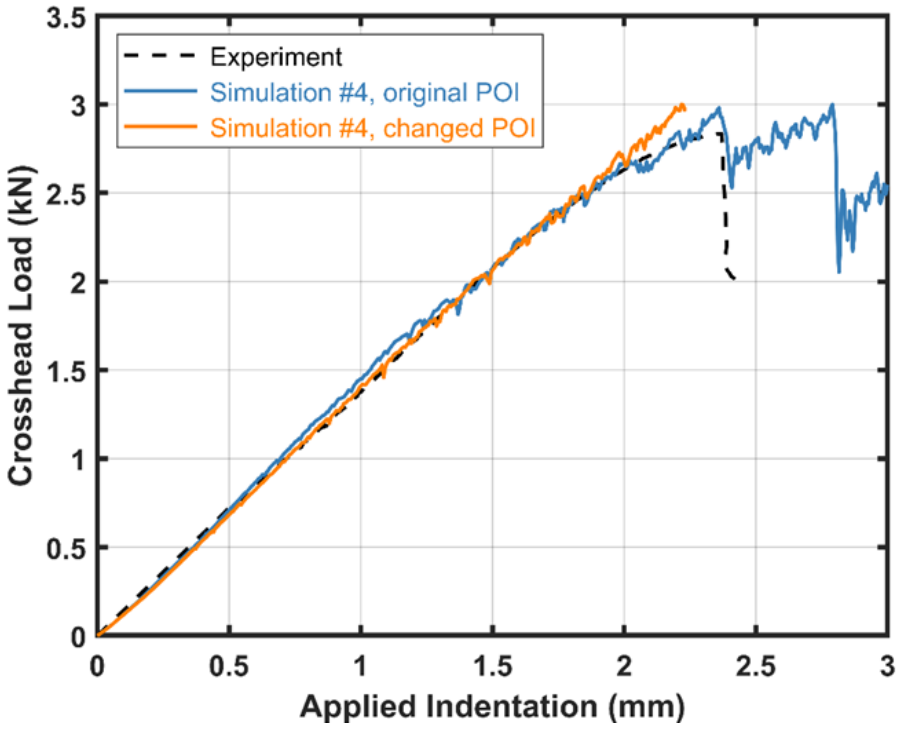

Fig. C-2 Effect on the load-displacement response of Simulation 4 by changing the POI. Simulation with the changed POI (orange curve) aborted early at u_y = 2.23 mm due to element distortion.

Changing the POI location had only a negligible effect in the initial, linear portion of the simulation. The location influenced the load-displacement response in the nonlinear regime, likely due to different sequences of failing elements. However, as shown in Fig. C-3, while there was a difference in the exact position of failed elements, the overall directional trend of failure remained the same. Both simulations had two crack systems oriented at approximately 45° to the y = 0 horizontal line.

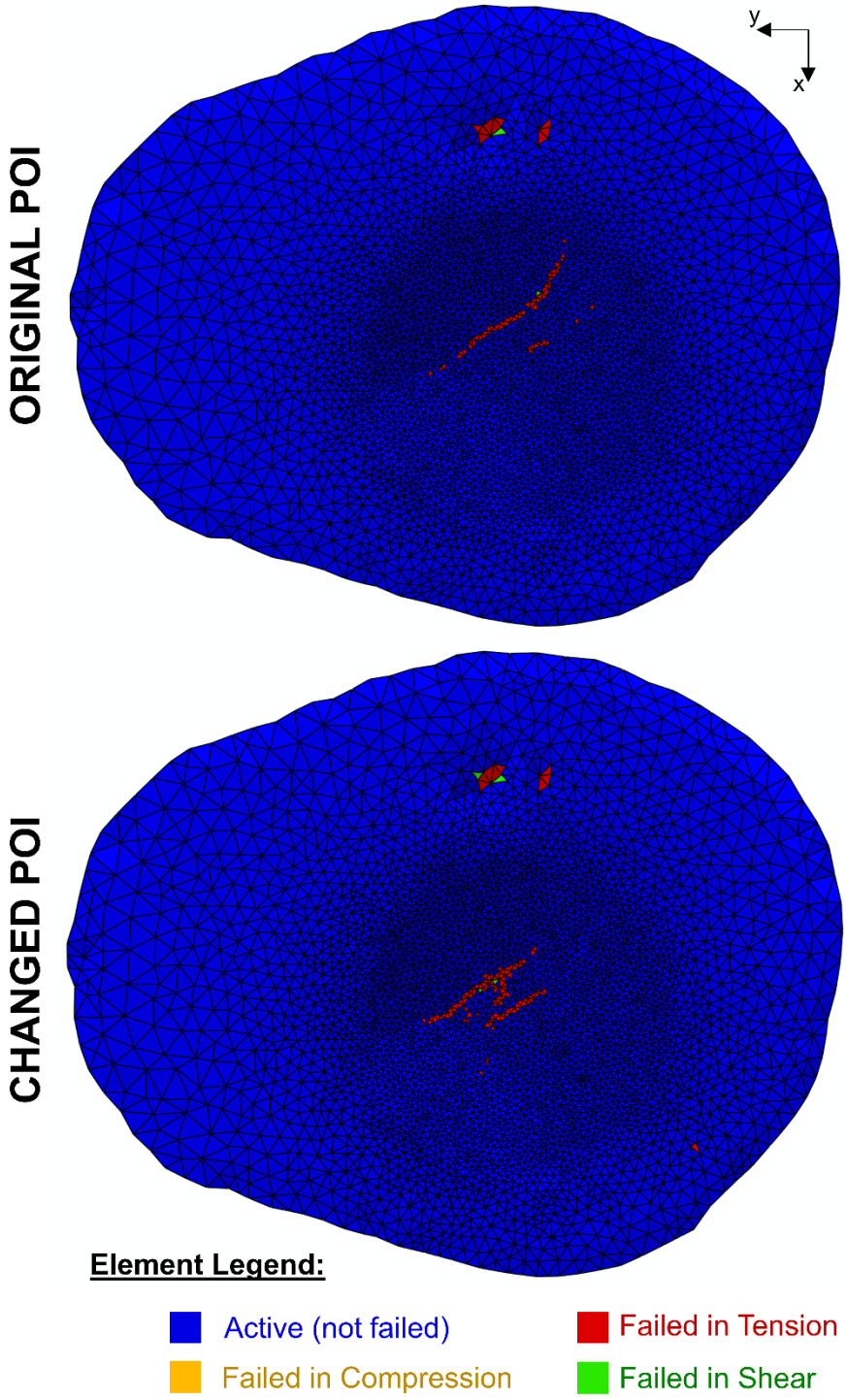

Fig. C-3 Effect on the backface cracking pattern of changing the POI. The meshes are in the undeformed configuration prior to the start of the simulation. Elements are color-coded by active/failed status for the time point corresponding to an applied displacement of $u_y = 2.23$ mm.

List of Symbols, Abbreviations, and Acronyms

2-D	two-dimensional
3-D	three-dimensional
ARL	Army Research Laboratory
BVF	bone volume fraction
CT	computed tomography
D_{eff}	effective diameter
DEVCOM	US Army Combat Capabilities Development Command
FE	finite element
HEMC	hybrid experimental-modeling-computational
IE	internal energy
IT	inner table
KE	kinetic energy
M	mechanism
MIMB	microstructurally inspired mechanism-based
MIS	Mimics Innovation Suite
NIH	National Institutes of Health
OT	outer table
POI	point of indentation/impact
R_{curv}	radius of curvature
SDV	state-dependent variable
V_{proj}	velocity
VUMAT	(vectorized) user-specified material subroutine

1 (PDF) DEFENSE TECHNICAL INFORMATION CTR
DTIC OCA

1 (PDF) DEVCOM ARL
FCDD RLD DCI
TECH LIB

1 (PDF) DEVCOM ARL ARO
FCDD RLR
D STEPP

11 (PDF) CCDC NATICK SOLDIER SYSTEMS CTR
M G CARBONI
D COLANTO
R DILLALLA
B FASEL
J FONTECCHIO
B KIMBALL
J KIREJCZYK
J PARKER
M MAFEO
M MARKEY
D PHELPS

3 (PDF) PROG EXECUTIVE OFC SOLDIER
J HOPPING
J MULLENIX
D OTTERSON

1 (PDF) US ARMY TEST AND EVALUATION COMMAND
A FOURNIER

1 (PDF) MTRL SCIENCES DIV
LAWRENCE BERKELY NATL LAB
R RITCHIE

5 (PDF) SOUTHWEST RSRCH INST
C ANDERSON JR
S CHOCRON
D NICOLELLA
T HOLMQUIST
G JOHNSON

2 (PDF) NIST
A FORSTER
M VANLANDINGHAM

1 (PDF) INST FOR DEFNS ANLYS
Y MACHERET

3 (PDF) MRMC DOD BLAST INJURY RSRCH PROGRAM COOR OFC
R GUPTA
T PIEHLER
R SHOGE

2 (PDF) MRMC JTAPIC PRGM OFC
W LEI
J USCILOWICZ

1 (PDF) WIAMAN PMO
K LOFTIS

4 (PDF) US ARMY AEROMEDICAL RSRCH LAB
F BROZOSKI
V CHANCEY
B MCENTYRE
D WISE

1 (PDF) CCDC GROUND VEHICLE SYSTEMS CENTER
R SCHERER

1 (PDF) CCDC
AMSRD PE
D RUSIN

2 (PDF) CCDC CHEMICAL BIOLOGICAL CENTER
M HORSMON
N VINCELLI

1 (PDF) OSD DOT&E
J IVANCIK

5 (PDF) US NAVAL RESEARCH LABORATORY
A BAGCHI
A ILIOPOULOS
J MICHOPOULOS
K TEFERRA
X TAN

3 (PDF) CCDC DAC
FCDD DAS LBW
G DIETRICH
FCDD DAS LBE
J GURGANUS
S SNEAD

88 (PDF) DEVCOM ARL
FCDD RLW
S KARNA
J NEWILL
A RAWLETT
S SCHOENFELD
J ZABINSKI
FCDD RLW B
R BECKER
J CAMPBELL
P GILLICH
C HOPPEL
B SCHUSTER
A TONGE
L VARGAS-GONZALEZ
FCDD RLW L
A DAGRO
A EIDSMORE
C GOOD
T V SHEPPARD
T THADDEUS
FCDD RLW LF
T G BROWN
FCDD RLW LH
T EHLERS
L MAGNESS
C MEYER
D SCHEFFLER
FCDD RLW
J BEATTY
J MCCAULEY
FCDD RLW M
E CHIN
FCDD RLW MA
T BOGETTI
T PLAISTED
J SANDS
E WETZEL
M YEAGER
C YEN
FCDD RLW MB
G GAZONAS
B LOVE
P MOY
D O'BRIEN
J SIETINS
J SUN
T WALTER
FCDD RLW MC
R JENSEN
FCDD RLW MD
A BUJANDA
B CHEESEMAN
K CHO
J LA SCALA
S WALSH
FCDD RLW ME
J LASALVIA
P PATEL
S SILTON
J SWAB
FCDD RLW MF
K DARLING
S GRENDAHL
H MURDOCH
FCDD RLW MG
J ANDZELM
J LENHART
R MROZEK
FCDD RLW P
R FRANCART
FCDD RLW PA
S BILYK
FCDD RLW PB
S ALEXANDER
T BAUMER
A BROWN
B FAGAN
A GOERTZ
A GUNNARSSON
C HAMPTON
M KLEINBERGER
E MATHEIS
J MCDONALD
P MCKEE
K RAFAELS
S SATAPATHY
M TEGTMEYER
T WEERASOORIYA
S WOZNIAK
T ZHANG
FCDD RLW PC
J CAZAMIAS
D CASEM
J CLAYTON
C MEREDITH
L SHANNAHAN
J LLOYD
FCDD RLW PD
R DONEY
K MASSER
C RANDOW
FCDD RLW PE
M LOVE
P SWOBODA
FCDD RLW PF
N GNIAZDOWSKI
R GUPTA
S KUKUCK
FCDD RLW S
A WEST

4 (PDF) WHITING SCHOOL OF ENG
JOHNS HOPKINS UNIV
KT RAMESH
T D NGUYEN
B NOTGHI
S BAILOOR

2 (PDF) COULTER DEPT OF BIOMED ENG
GEORGIA INST OF TECH
S MARGULIES
D MCDOWELL

1 (PDF) DEPT OF ENGRNG SCI AND MECHANICS
VIRGINIA POLYTECHNIC INST AND STATE UNIV
R BATRA

3 (PDF) MASSACHUSETTS INST OF TECHLGY
INST FOR SOLDIER NANOTECHNOLOGIES
R RADOVITZKY
S SOCRATE
M J BUEHLER

1 (PDF) DEPT OF MECHL AND NUCLEAR ENGRNG
THE PENNSYLVANIA STATE UNIV
R KRAFT

1 (PDF) INDIAN INST OF TECH
R BHARDWAJ

2 (PDF) CENTER FOR APPLIED BIOMECHANICS
UNIV OF VIRGINIA
R SALZAR
M B PANZER

1 (PDF) UCSD MAT SCI AND ENG
MARC MEYERS

1 (PDF) DUKE UNIV
BIOMED ENG
CR BASS

1 (PDF) UNIV OF CAPE TOWN
BLAST IMPACT & SURVIVABILITY UNIT
TJ CLOETE

1 (PDF) UNIV OF OXFORD
BLAST IMPACT & SURVIVABILITY UNIT
C SIVIOUR

1 (PDF) UNIV OF CAMBRIDGE
ENG DEPT
V DESHPANDE

4 (PDF) UNIV OF SOUTH CAROLINA
COL OF ENG
S RAJAN
M SUTTON
S SOCKALINGAM
F THOMAS

1 (PDF) IMPERIAL COL LONDON
DEPT OF PHYSICS
W PROUD

1 (PDF) DIV OF ENG AND APPL SCI
CALTECH
R RAVICHANDRAN

1 (PDF) DEPT OF AERO ENG AND ENG MECH
U TEXAS AUSTIN
K RAVI-CHANDAR

1 (PDF) AERO AND ASTRO ENG
PURDUE UNIV
W CHEN

1 (PDF) DEPT OF NEUROSURGERY
MED COL OF WISCONSIN
N YOGANANDAN